

Accepted Manuscript

Three-dimensional Concrete Impact and Penetration Simulations Using the Smoothed Particle Galerkin Method

C.T. Wu , Youcai Wu , John E. Crawford , Joseph M. Magallanes

PII: S0734-743X(16)30843-0
DOI: [10.1016/j.ijimpeng.2017.03.005](https://doi.org/10.1016/j.ijimpeng.2017.03.005)
Reference: IE 2861



To appear in: *International Journal of Impact Engineering*

Received date: 24 October 2016
Revised date: 27 February 2017
Accepted date: 3 March 2017

Please cite this article as: C.T. Wu , Youcai Wu , John E. Crawford , Joseph M. Magallanes , Three-dimensional Concrete Impact and Penetration Simulations Using the Smoothed Particle Galerkin Method, *International Journal of Impact Engineering* (2017), doi: [10.1016/j.ijimpeng.2017.03.005](https://doi.org/10.1016/j.ijimpeng.2017.03.005)

This is a PDF file of an unedited manuscript that has been accepted for publication. As a service to our customers we are providing this early version of the manuscript. The manuscript will undergo copyediting, typesetting, and review of the resulting proof before it is published in its final form. Please note that during the production process errors may be discovered which could affect the content, and all legal disclaimers that apply to the journal pertain.

Highlights

- Three dimensional smooth particle Galerkin formulation is presented
- An adaptive anisotropic Lagrangian kernel is utilized
- A bond-based failure criterion is introduced
- A frictionless self-contact algorithm has been developed
- Numerical results are validated with test data for high velocity impact penetration on concrete structures

Three-dimensional Concrete Impact and Penetration Simulations Using the Smoothed Particle Galerkin Method

C.T. Wu^{1*}, Youcai Wu¹, John E. Crawford², Joseph M. Magallanes²

¹ Livermore Software Technology Corporation, 7374 Las Positas Rd., Livermore, CA 94551, USA

² Karagozian & Case Inc., 700 N. Brand Blvd, Suite 700, Glendale, CA 91203

Abstract

In this paper, we model the three-dimensional concrete impact and penetration problems using a stabilized meshfree method. The present method is established using a non-residual penalty term from strain smoothing as a means of stabilizing the meshfree nodal integration method under the Galerkin framework. As a result, the meshfree discretization leads to a dual stress point algorithm with the stabilization parameterized by a measure of a local length scale. An adaptive anisotropic Lagrangian kernel is considered in junction with the stabilized meshfree formulation for the severe deformation analysis. In order to avoid the spurious damage growth and material self-healing in concrete failure analysis, a bond-based failure criterion is introduced. A frictionless self-contact algorithm is also developed to model the interaction between concrete debris in damage. Several impact examples are investigated including the study of scabbing and perforation of concrete under high velocity impact. The numerical results are compared with the experimental data to demonstrate the effectiveness of the present method.

Keywords: Smoothed particle Galerkin; Impact penetration; Concrete; Meshfree

1. Introduction

The necessity to model the severe deformation followed by moving discontinuities in three-dimensional concrete impact and penetration problems makes numerical simulation extremely difficult by the conventional mesh-based numerical methods such as the Lagrangian finite element method. Although the Eulerian description for fluid mechanics applications can be easily adopted to circumvent the mesh distortion problem encountered in the Lagrangian formulation, the Eulerian representation of material flow presents other numerical difficulties in tracking the material points and free surfaces in concrete impact and penetration simulations. Alternatively, the arbitrary Lagrangian Eulerian (ALE) algorithm [1] advances the mesh independently with material flow and makes it possible to take into account the movements of free surfaces while reducing mesh distortion. Regardless of this distinct property offered by ALE method, its shortcoming is the occurrence of numerical oscillations when the convective effect is dominant

*Corresponding author, Wu CT, E-mail: ctwu@lstc.com

in the governing equations. This numerical instability often arises in impact and penetration simulation when the velocity difference between the mesh movements and medium flow becomes evident. As a generalization of Eulerian approach, the ALE method also has difficulty to model the formation of new surfaces in the course of perforation and fragmentation processes.

Meshfree methods, on the other hand, offer diverse numerical advantages over the conventional mesh-based numerical methods in modeling large deformation [2, 3], moving discontinuity [4] and immersed problems [5]. Meshfree methods can be roughly categorized into discontinuous and continuous approaches. The Discrete Element Method (DEM) [6] is a representative discontinuous meshfree method based on the contact interactions between discrete grains to model the motion of granular materials. In contrast to DEM that describes the problem at particle scale, the majority of meshfree methods belong to the continuous approach that discretizes the problem at a field-scale level [7]. In essence, the material behavior in continuous meshfree methods is endowed with the conservation properties (mass, momentum and energy), and the uniqueness and convergence of solutions are ensured under appropriate variational principle and relevant field approximations. Especially, an accurate constitutive model for continuous meshfree methods is desired to obtain sufficient information of stress and deformation fields for capturing the fundamental structure response as well as the projectile characteristics in concrete impact and penetration simulations.

The earliest development in the continuous meshfree methods is the Smoothed Particle Hydrodynamics (SPH) method. The foundation of the SPH method is the kernel estimate introduced by Monaghan [8]. In SPH method, partial differential equations are transformed into integral equations and the kernel estimate then provides the approximation to estimate the field variables at the discrete particles. Since the functions are evaluated at the particles, the use of a mesh is no longer required. This ability to handle severe deformations without the use of meshes in fluid-like motion allows the SPH method to be applied to problems that historically have been reserved for Eulerian approaches [9]. In spite of that, a direct application of SPH method to solid mechanics problems is known to suffer numerous numerical deficiencies [10, 11], namely the lack of approximation consistency, tension instability, presence of spurious low-energy modes, dispersive wave propagation, complication in enforcing the essential boundary conditions, difficulty to represent the crack surface in 3D problem and inability to prevent the material self-healing in failure analysis. While many SPH models [12 -14] have been utilized to simulate the severe deformation and material failure in concrete impact and penetration problems, less attention [7, 15, 16] was paid to the improvement of the unstable results induced by those numerical deficiencies.

In the past two decades, many advanced meshfree Galerkin methods were developed to resolve some of the numerical issues in SPH method. Among them, Element-free Galerkin (EFG) [17] and Reproducing Kernel Particle Method (RKPM) [18] are two earliest meshfree methods to tackle the issues of approximation consistency and boundary conditions in SPH method. In addition to the improvement of approximation consistency, a Galerkin-based SPH formulation [19] was developed to intensify the formulation consistency for the analysis of free surface flows. In the meantime, the Cracking Particles Method (CPM) was developed [20] to provide a simple way for the description of evolving cracks in brittle fracture analysis. As an alternative to the visibility method [1] and the methods based on geometric information or screening effects [22], a discontinuous representation of the crack surface in CPM is delineated through the enrichment of step function at cracking particles. This unique feature of CPM makes it attractive to model the complex fracture behavior in three-dimensional case. The Stabilized

Conforming Nodal Integration (SCNI) method [23] is another representative meshfree method introduced to ameliorate the spurious low-energy modes present in meshfree direct nodal integration scheme. The SCNI technique was later generalized to higher order strain smoothing by Duan *et al.* [24] to achieve cubic rates of convergence in the L^2 norm for the linear analysis. Arbitrary high order Galerkin exactness for SCNI method was also derived [25] under the general framework of variational consistency for improving the integration errors in meshfree methods. In the meantime, different integration schemes [26, 27] based on SCNI method also have been proposed to enhance the numerical stability of SCNI method. A modification of SCNI algorithm to the stabilized non-conforming nodal integration (SNNI) scheme [28] also has been developed to bypass the need of constructing the conforming smoothing cells for nodal integration. Despite the irreconcilable demands on the stabilization control parameter placed by the accuracy requirement, the SNNI scheme has been successfully applied to the model of the concrete impact and penetration problems [29]. Several regularized meshfree methods [30 – 32] were also developed based on the concept of SCNI method for the material failure analysis. Nevertheless, most meshfree methods cannot preclude the use of background mesh or smoothing cells, thus pose significant challenges from both the mathematical formulation and the programming aspects in the three-dimensional simulation of severe deformation and material failure problems.

The Smoothed Particle Galerkin (SPG) method [33, 34] recently introduced by Wu *et al.* is a new continuous meshfree method that aims to bypass the need of background mesh, reveal a proper stabilization setting and guide the development of practical nodal integration schemes for severe deformation problems. The essence of SPG method is an introduction of strain operator for stabilization. Most notably, the strain operator is invertible stable and well-defined in the severe deformation analysis [34]. In the earliest SPG method [33], the strain operator is defined through a strain gradient stabilization (SGS) scheme [33, 34]. In SGS scheme, the first-order strain gradients are derived based on the decomposed strain field from the displacement smoothing. In the subsequent SPG method [35, 36], the first-order strain gradients are derived based on a direct strain smoothing leading to a penalty-based h^2 -stabilization formulation. As opposed to the residual type stabilization [28, 37], the SPG stabilization formulation is a non-residual type in which the penalized stabilization functional is parameterized by a measure of the local length scale without a need of stabilization control parameter. Following that, an incorporation of second-order strain gradients in the SPG formulation has led to a development of the regularized SPG method [35] for the analysis of damage-induced strain localization problem in elastic materials. Most recently, a particle insertion-deletion scheme [36] has been introduced to the regularized SPG method to substantially model the ductile fracture in two-dimensional explicit dynamics analysis.

The scope of this paper is to present an improved SPG method for the prediction of fundamental structure response and projectile characteristics in the three-dimensional concrete impact and penetration problems. The present method combines our previous development in two-dimensional large deformation analysis [34] and several numerical enhancements in failure analysis. The outline of the paper is organized as follows: An overview of smoothed particle Galerkin method for large deformation analysis is given in Section 2. The corresponding three-dimensional discrete equations and resulting dual stress point algorithm for spatial integration are described in Section 3. The adoption of adaptive anisotropic Lagrangian kernel in the three-dimensional formulation is also described in the same section. Section 4 presents a regularized concrete damage model. The consideration of bond-based failure and self-contact between

damage particles also is discussed in Section 4. Numerical examples are presented in Section 5, and finally the conclusions are made in Section 6.

2. Overview on the SPG method

Consider a three-dimensional body $\Omega^0 \subset R^3$ defined in the reference configuration. The image of Ω^0 is the current domain denoted by Ω , and the motion Φ is described by $\mathbf{x} = \Phi(\mathbf{X}, t)$, where $t \in [0, T]$ is the time, \mathbf{X} and \mathbf{x} are material and spatial coordinates, respectively. The strong form of the dynamic problem can be stated by the following [38]:

$$\sigma_{ij,j} + b_i = \rho \ddot{u}_i \text{ in } \Omega \quad (1)$$

$$u_i = g_i \text{ on } \Gamma_g \quad (2)$$

$$\sigma_{ij} n_j = h_i \text{ on } \Gamma_h \quad (3)$$

where σ_{ij} is the Cauchy stress tensor, ρ is material density, b_i is the component of body force, u_i is the displacement component, g_i is the prescribed boundary displacement, n_i is the unit outward normal vector, h_i is the traction imposed on Neumann boundary. We also have $\partial\Omega = \Gamma = \Gamma_g \cup \Gamma_h$ and $\Gamma_g \cap \Gamma_h = 0$ denoting the Lipschitz continuous boundary.

In SPG method [33 – 36], the stabilization strain field is introduced to the standard variational formulation through a penalty approach. For simplicity, we assume the homogenous Dirichlet problem in the following variational derivation. The admissible space for the displacement fields is defined by

$$V^h(\Omega) = \{v : v|_{\Omega} \in H^1(\Omega), v = 0 \text{ on } \partial\Omega\} \quad (4)$$

where H^1 is the Sobolev space of degree one that is regular enough to make the variational problem well-defined.

For a particle distribution denoted by an index set $Z_I = \{\mathbf{x}_I\}_{I=1}^{NP}$, we approximate the displacement field using the meshfree approximation to give

$$\mathbf{u}^h(\mathbf{x}) = \sum_{I=1}^{NP} \phi_I^a(\mathbf{x}) \tilde{\mathbf{u}}_I \equiv \hat{\mathbf{u}}(\mathbf{x}) \quad \forall \mathbf{x} \in \Omega \quad (5)$$

where NP is the total number of particles in discretization. $\phi_I^a(\mathbf{x})$, $I=1, \dots, NP$ can be considered as the shape functions of the meshfree approximation for displacement field $\mathbf{u}^h(\mathbf{x})$. Note that the radius size a of $\phi_I^a(\mathbf{x})$ is a numerical length parameter in meshfree displacement approximation. In general, $\tilde{\mathbf{u}}_I$ is not the physical particle displacement and is often referred to as the “generalized displacement” [2] of particle I in Galerkin meshfree method. As a result, special essential boundary condition treatment is needed. In order to simplify the enforcement of essential boundary condition in this study, a first-order meshfree convex approximation [39] is considered. They are constructed by the Generalized Meshfree Approximation (GMF) method

(see [39] for detail mathematical derivation and [40] for the nonlinear formulations in general solid mechanics applications). The most recent development of meshfree convex approximation can also be found in [41, 42]. With the meshfree convex approximation, we can define the \mathbf{H}_0^1 -conforming subspace for the approximation of displacement field to be

$$\mathbf{V}^h := \text{span} \left\{ \phi_I^a \mid \left(\text{supp } \phi_I^a \right)^p \subset \Omega, I \in Z_I \right\} \quad (6)$$

Using the defined approximation space, the weak form for the given problem can be obtained based on the penalized variational formulation [33 – 36] through an updated Lagrangian approach with reference to the current configuration. The weak form problem is to find $\hat{\mathbf{u}}(\mathbf{x}) \in \mathbf{V}^h$ such that the first variation in the energy is zero:

$$\delta W = \delta W_{\text{int}} - \delta W_{\text{ext}} + \delta W_{\text{inertia}} + \delta W_{\text{penalty}} = 0 \quad \forall \delta \hat{\mathbf{u}} \in \mathbf{V}^h \quad (7)$$

with

$$\delta W_{\text{int}} = \int_{\Omega} \delta \nabla \hat{\mathbf{u}} : \boldsymbol{\sigma}(d) d \Omega \quad (8)$$

$$\delta W_{\text{ext}} = \int_{\Omega} \delta \hat{\mathbf{u}} \cdot \mathbf{b} d \Omega + \int_{\Gamma_h} \delta \hat{\mathbf{u}} \cdot \mathbf{h} d \Gamma \quad (9)$$

$$\delta W_{\text{inertia}} = \int_{\Omega} \delta \hat{\mathbf{u}} \cdot \ddot{\rho} \hat{\mathbf{u}} d \Omega \quad (10)$$

$$\delta W_{\text{penalty}} = \int_{\Omega} \delta \left(\nabla^2 \hat{\mathbf{u}} \cdot \boldsymbol{\lambda}^b(\mathbf{x}) \right) : \tilde{\boldsymbol{\sigma}} d \Omega \quad (11)$$

where ∇ is the spatial gradient. $\boldsymbol{\sigma}(d)$ is the Cauchy stress obtained by direct nodal integration scheme and d is a monotonic increasing scalar damage variable introduced by the damage law in concrete model which will be described in Section 4. $\boldsymbol{\lambda}^b$ is the coefficient matrix for stabilization and is given by [35, 36]

$$\boldsymbol{\lambda}^b(\mathbf{x}) = \int_{\Omega} \tilde{\Psi}^b(\mathbf{x}; \boldsymbol{\xi}) (\boldsymbol{\xi} - \mathbf{x}) d \Omega \quad (12)$$

where $\tilde{\Psi}^b$ is the strain smoothing function for stabilization in meshfree nodal integration method, $\tilde{\Psi}^b(\mathbf{r}) > 0$ for $\|\mathbf{r}\| < b$, $\tilde{\Psi}^b(\mathbf{r}) = 0$ for $\|\mathbf{r}\| \geq b$, and subscript b denotes the radius of three-dimensional influence domain for the strain smoothing function [35, 36]. In this study $a = b$ (for stabilization) is used for all numerical investigations. The penalty term $\delta W_{\text{penalty}}$ in Eq. (11) contains an enhanced stress field $\tilde{\boldsymbol{\sigma}}$ for stabilization. Note that stress quantities in Eq. (11) are defined in the current configuration Ω .

Considering that the Lagrangian meshfree shape function [2, 34, 36] and the gradients of displacement and strain approximations are defined in the reference configuration to avoid the tensile instability and dispersive wave propagation, the variation equations of Eqs. (8) ~ (11) are transformed from the current configuration Ω to the reference configuration Ω^0 as

$$\int_{\Omega^0} \delta \hat{u}_i \rho^0 \ddot{u}_i d\Omega = \int_{\Omega^0} \frac{\partial \delta \hat{u}_i}{\partial X_k} F_{kj}^{-1} \sigma_{ij} J^0 d\Omega \quad (13)$$

$$+ \int_{\Omega^0} F_{im}^{-T} \frac{\partial^2 \delta \hat{u}_i}{\partial X_m \partial X_n} F_{nk}^{-1} \lambda_k^b(\mathbf{x}) \tilde{\sigma}_{ij} J^0 d\Omega - l^{ext}(\hat{\mathbf{u}})$$

$$l^{ext}(\hat{\mathbf{u}}) = \int_{\Omega^0} \delta \hat{\mathbf{u}} \cdot \mathbf{b} d\Omega + \int_{\Gamma_f^0} \delta \hat{\mathbf{u}} \cdot \mathbf{h}^0 d\Gamma \quad (14)$$

$$J^0 = \det(\mathbf{F}), F_{ij}(\mathbf{X}) = \frac{\partial x_i(\mathbf{X})}{\partial X_j} = \sum_{l=1}^{NP} \frac{\partial \phi_l^a(\mathbf{X})}{\partial X_j} x_{li} \quad (15)$$

where \mathbf{F} is the deformation gradient, x_{li} denotes the i -component of current position at node l , and $\mathbf{X}=[X, Y, Z]^T$ is a position vector defined in the reference configuration. J^0 is the determinant of the deformation gradient.

3. Spatial Discretization

Using the first-order meshfree convex approximation [39, 40] for $\phi^a(\mathbf{X})$ and zero-order strain smoothing function for $\tilde{\psi}^b(\mathbf{X})$ leads to the following discrete form of momentum equation to be solved for explicit dynamics analysis in three-dimensional problem:

$$\mathbf{M}^{lump} \ddot{\mathbf{U}} = \mathbf{f}^{ext} - \mathbf{f}^{int} - \tilde{\mathbf{f}}^{stab} \quad (16)$$

$$\mathbf{M}_I^{lump} = \sum_{N=1}^{NP} \rho^0 \phi_I^a(\mathbf{X}_N) V_N^0 \mathbf{I}_{[3 \times 3]} \quad (17)$$

where \mathbf{f}^{ext} is standard external force matrix, $\ddot{\mathbf{U}}$ is the matrix contains nodal accelerations. V_K^0 is the initial nodal volume of node K , and \mathbf{M}_I^{lump} is the lumped nodal mass matrix. The internal force matrix is computed by the direct nodal integration scheme as

$$\mathbf{f}_I^{int} = \sum_{N=1}^{NP} \mathbf{B}_I^T(\mathbf{X}_N) \mathbf{A}(\mathbf{X}_N) \boldsymbol{\sigma}(\mathbf{X}_N) J^0 V_N^0 \quad (18)$$

$$\mathbf{B}_I(\mathbf{X}) = \begin{bmatrix} b_{I1}(\mathbf{X}) & 0 & 0 \\ 0 & b_{I2}(\mathbf{X}) & 0 \\ 0 & 0 & b_{I3}(\mathbf{X}) \\ b_{I2}(\mathbf{X}) & 0 & 0 \\ 0 & b_{I3}(\mathbf{X}) & 0 \\ 0 & 0 & b_{I1}(\mathbf{X}) \\ b_{I3}(\mathbf{X}) & 0 & 0 \\ 0 & b_{I1}(\mathbf{X}) & 0 \\ 0 & 0 & b_{I2}(\mathbf{X}) \end{bmatrix} \quad (19)$$

$$b_{I1}(\mathbf{X}) = \phi_{I,x}^a(\mathbf{X}), b_{I2}(\mathbf{X}) = \phi_{I,y}^a(\mathbf{X}) \text{ and } b_{I3}(\mathbf{X}) = \phi_{I,z}^a(\mathbf{X}) \quad (20)$$

$$\mathbf{A} = \begin{bmatrix} F_{11}^{-1} & 0 & 0 & F_{12}^{-1} & 0 & F_{13}^{-1} \\ 0 & F_{22}^{-1} & 0 & F_{21}^{-1} & F_{23}^{-1} & 0 \\ 0 & 0 & F_{33}^{-1} & 0 & F_{32}^{-1} & F_{31}^{-1} \\ F_{21}^{-1} & 0 & 0 & F_{22}^{-1} & 0 & F_{23}^{-1} \\ 0 & F_{32}^{-1} & 0 & F_{31}^{-1} & F_{33}^{-1} & 0 \\ 0 & 0 & F_{13}^{-1} & 0 & F_{12}^{-1} & F_{11}^{-1} \\ F_{31}^{-1} & 0 & 0 & F_{32}^{-1} & 0 & F_{33}^{-1} \\ 0 & F_{12}^{-1} & 0 & F_{11}^{-1} & F_{13}^{-1} & 0 \\ 0 & 0 & F_{23}^{-1} & 0 & F_{22}^{-1} & F_{21}^{-1} \end{bmatrix} \quad (21)$$

Finally, the stabilized force matrix is also computed by the direct nodal integration scheme as

$$\tilde{\mathbf{f}}_I^{stab} = \sum_{N=1}^{NP} \mathbf{F}^{-T}(\mathbf{X}_N) \tilde{\mathbf{B}}_I^T(\mathbf{X}_N) \tilde{\boldsymbol{\sigma}}(\mathbf{X}_N) \mathbf{J}^0 \mathbf{V}_N^0 \quad (22)$$

The first-order strain-gradient matrix $\tilde{\mathbf{B}}_I$ in Eq. (22) is given by

$$\tilde{\mathbf{B}}_I(\mathbf{X}) = \begin{bmatrix} \tilde{b}_{I1}(\mathbf{X}) & 0 & 0 \\ 0 & \tilde{b}_{I2}(\mathbf{X}) & 0 \\ 0 & 0 & \tilde{b}_{I3}(\mathbf{X}) \\ \tilde{b}_{I2}(\mathbf{X}) & \tilde{b}_{I1}(\mathbf{X}) & 0 \\ \tilde{b}_{I3}(\mathbf{X}) & 0 & \tilde{b}_{I1}(\mathbf{X}) \\ 0 & \tilde{b}_{I3}(\mathbf{X}) & \tilde{b}_{I2}(\mathbf{X}) \end{bmatrix} \quad (23)$$

The components of the first-order strain-gradient matrix $\tilde{\mathbf{B}}_I$ are

$$\tilde{b}_{I1}(\mathbf{X}) = \lambda_x^b(\mathbf{X}) \phi_{I,xx}^a(\mathbf{X}) + \lambda_y^b(\mathbf{X}) \phi_{I,xy}^a(\mathbf{X}) + \lambda_z^b(\mathbf{X}) \phi_{I,xz}^a(\mathbf{X}) \quad (24)$$

$$\tilde{b}_{I2}(\mathbf{X}) = \lambda_x^b(\mathbf{X}) \phi_{I,yx}^a(\mathbf{X}) + \lambda_y^b(\mathbf{X}) \phi_{I,yy}^a(\mathbf{X}) + \lambda_z^b(\mathbf{X}) \phi_{I,yz}^a(\mathbf{X}) \quad (25)$$

$$\tilde{b}_{I3}(\mathbf{X}) = \lambda_x^b(\mathbf{X}) \phi_{I,zx}^a(\mathbf{X}) + \lambda_y^b(\mathbf{X}) \phi_{I,zy}^a(\mathbf{X}) + \lambda_z^b(\mathbf{X}) \phi_{I,zz}^a(\mathbf{X}) \quad (26)$$

$$\lambda_x^b(\mathbf{X}) = \sum_{J=1}^{NP} \tilde{\Psi}_J^b(\mathbf{X})(X_J - X) \quad (27)$$

$$\lambda_y^b(\mathbf{X}) = \sum_{J=1}^{NP} \tilde{\Psi}_J^b(\mathbf{X})(Y_J - Y) \quad (28)$$

$$\lambda_z^b(\mathbf{X}) = \sum_{J=1}^{NP} \tilde{\Psi}_J^b(\mathbf{X})(Z_J - Z) \quad (29)$$

$\tilde{\boldsymbol{\sigma}}^T = (\tilde{\sigma}_{11}, \tilde{\sigma}_{22}, \tilde{\sigma}_{33}, \tilde{\sigma}_{12}, \tilde{\sigma}_{13}, \tilde{\sigma}_{23})$ is a vector containing the component of Cauchy stress associated with the stabilization. Note that $\phi_{I,xy}^a = \phi_{I,yx}^a$, $\phi_{I,xz}^a = \phi_{I,zx}^a$ and $\phi_{I,yz}^a = \phi_{I,zy}^a$. In explicit dynamics analysis, the nodal stabilized stress vector [35, 36] is updated using the incremental stabilized

stress vector computed according to the suggestion of Belytschko and Lee [44] and is given in large strain by

$$\tilde{\sigma}_{n+1} = \bar{\sigma}_{n+1} + \Delta \tilde{\sigma}_{n+1}^J \Delta t \quad (30)$$

The Jaumann stress rate of the Cauchy stress for stabilization is

$$\Delta \tilde{\sigma}_{n+1}^J = 2\tilde{G}(1-d)(\tilde{\mathbf{B}}_{dev})\Delta \mathbf{v}_{n+1} - \mathbf{W} \cdot \tilde{\sigma}_n + \tilde{\sigma}_n \cdot \mathbf{W} \quad (31)$$

where \mathbf{W} is spin tensor. $\bar{\sigma}_{n+1} = \mathbf{Q}_{n+1} \cdot \tilde{\sigma}_n \cdot \mathbf{Q}_{n+1}^T$ follows the Hughes and Winget [45] incrementally objective integration scheme and \mathbf{Q} is the incremental rotation tensor. \tilde{G} is called the “modified shear modulus” [44] which is computed by

$$2\tilde{G} = \sqrt{\frac{H_{\Delta\tau}}{H_{\Delta e}}} \quad (32)$$

$$H_{\Delta\tau} = \frac{1}{2} \sum_{i=1}^3 \sum_{j=1}^3 \Delta \tau_{ij} \Delta \tau_{ij}, H_{\Delta e} = \frac{1}{2} \sum_{i=1}^3 \sum_{j=1}^3 \Delta e_{ij} \Delta e_{ij} \quad (33)$$

$\Delta \tau_{ij}$ and Δe_{ij} are the components of deviatoric part of the stress and strain increments, respectively, which are obtained from the regularized nodal stress and strain computation. $\tilde{\mathbf{B}}_{dev}$ is the deviatoric part of first-order strain-gradient matrix $\tilde{\mathbf{B}}$.

In order to handle the severe deformation that is beyond the applicability of Lagrangian shape function in Eq. (14), an adaptive anisotropic Lagrangian kernel is considered [34]. Using the chain rule, the calculation for the deformation gradient in Eq. (16) can be rewritten [34, 46] as

$$\mathbf{F}^{n+m} = \hat{\mathbf{F}}^{n+m} \mathbf{F}^n \quad (34)$$

where $\hat{\mathbf{F}}^{n+m}(\hat{\mathbf{x}})$ is the decomposed deformation gradient, from $t=t_n$ to t_{n+m} , computed based on the new reference configuration and is given by

$$\hat{F}_{ij}^{n+m}(\mathbf{X}_J) = \frac{\partial \hat{x}_i}{\partial \hat{X}_j} = \sum_{l=1}^{NP} \frac{\partial \Psi_l}{\partial \hat{X}_j}(\hat{\mathbf{X}}_J) \hat{x}_{il} \quad (35)$$

Here, $\hat{\mathbf{x}} = \hat{\mathbf{X}} + \tilde{\mathbf{u}}(\mathbf{X}, t_{n+m})$ is a position vector defined in the new reference configuration $\hat{\mathbf{X}} = \mathbf{x}(\mathbf{X}, t_n)$. Since this particle-based reconstruction step for the computation of deformation gradient does not involve remeshing as that in the r/h-adaptive finite element methods, the stress-recovery techniques and remapping procedures that interpolate the internal variables at the integration points from the old discretization to the new discretization are not necessary. This unique property of present method leads to a relatively simple mathematical formulation for

computer programming in terms of simulating the severe deformation in large-scale three-dimensional problems.

In this study, the adaptive anisotropic Lagrangian kernel is constantly updated over a period of time. In each new reference configuration, an ellipsoidal nodal support is defined for the neighbor particle searching. In three-dimensions, a local $\hat{\mathbf{X}}^I$ -coordinate system in which the axes are parallel to the global Cartesian coordinates and with its origin located at $\hat{\mathbf{X}}_I$ is defined for each meshfree node I as shown in Fig. 1. The ellipsoid of each meshfree node I is defined by another local $\hat{\hat{\mathbf{X}}}^I$ -coordinate system formed by a dyad of mutually perpendicular vectors \mathbf{h}_{ii}^n , $i=1, 2, 3$, the semi-major axes of the ellipsoid.

The three-dimensional ellipsoidal cubic spline kernel function can be defined in the local $\hat{\hat{\mathbf{X}}}^I$ -coordinate system by

$$\phi(\hat{\mathbf{X}}_J - \hat{\mathbf{X}}_I) = \phi_1\left(\frac{\hat{\hat{\mathbf{X}}}_J^I}{h_1^n}\right) \phi_1\left(\frac{\hat{\hat{\mathbf{Y}}}_J^I}{h_2^n}\right) \phi_1\left(\frac{\hat{\hat{\mathbf{Z}}}_J^I}{h_3^n}\right) \quad (36)$$

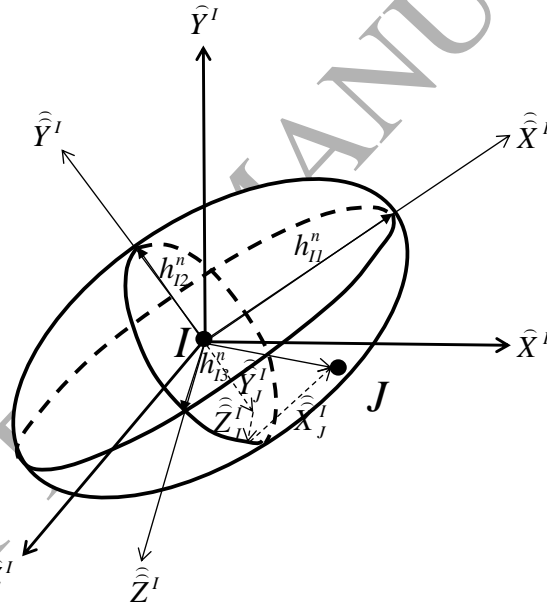


Fig. 1. Ellipsoidal nodal support in three-dimensional adaptive anisotropic Lagrangian kernel approach.

where $h_1^n = |\mathbf{h}_{11}^n|$, $h_2^n = |\mathbf{h}_{22}^n|$ and $h_3^n = |\mathbf{h}_{33}^n|$ are the semi-major axes of the ellipsoid. $\hat{\hat{\mathbf{X}}}_J^I$, $\hat{\hat{\mathbf{Y}}}_J^I$ and $\hat{\hat{\mathbf{Z}}}_J^I$ are the projections of relative position vector $\hat{\mathbf{X}}_J - \hat{\mathbf{X}}_I$ on the local $\hat{\hat{\mathbf{X}}}^I$ -coordinate system respectively. ϕ_1 is the standard one-dimensional cubic spline kernel function. In general, we have $h_1^0 = h_2^0 = h_3^0$ as a spherical shape cubic spline kernel function at $t=0$. The spherical shape domain of cubic spline kernel function deforms and rotates according to the Lagrangian motion between each two adaptive Lagrangian kernel steps. In this study, the evolution of ellipsoid is

determined by the right Cauchy-Green deformation tensor

$$\mathbf{G}^n = (\mathbf{F}^n)^T \cdot \mathbf{F}^n = \sum_{i=1}^3 (\lambda_i^n)^2 \mathbf{n}_i \otimes \mathbf{n}_i \quad (37)$$

where $\lambda_i^n, i=1,2,3$ are three distinct principal stretches and $\mathbf{n}_i = [n_{xi}, n_{yi}, n_{zi}]^T, i=1,2,3$ are the corresponding eigenvectors. Therefore, the length and direction of the semi-axes of ellipsoid are estimated by the eigenvalues and eigenvectors, respectively, of the matrix \mathbf{G}^n . In other words, the eigenvalues of \mathbf{G}^n represent three principal stretches of the ellipsoid at $t=t_n$. As a consequence, the semi-major axes of the ellipsoid are approximated by

$$h_1^n = \lambda_1^n h_1^0, h_2^n = \lambda_2^n h_2^0 \text{ and } h_3^n = \lambda_3^n h_3^0 \quad (38)$$

and the vectors $\mathbf{h}_i^n = h_i^n \mathbf{n}_i = h_i^n [n_{xi}, n_{yi}, n_{zi}]^T, i=1,2,3$ are obtained. The gradients of the three-dimensional ellipsoidal cubic spline kernel function needed in the computation of displacement-gradient matrix \mathbf{B} and the stabilized strain-gradient matrix $\tilde{\mathbf{B}}^{dev}$ can also be evaluated by

$$\begin{aligned} \nabla_{\hat{\mathbf{x}}} (\phi(\hat{\mathbf{X}}_J - \hat{\mathbf{X}}_I))_i &= \left(\frac{\mathbf{h}_i^n}{h_i^n} \right) \cdot \nabla_{\hat{\mathbf{x}}} (\phi(\hat{\mathbf{X}}_J - \hat{\mathbf{X}}_I)) \\ &= n_{xi} \frac{\partial \phi_1 \left(\frac{\hat{X}_J^I}{h_1^n} \right)}{\partial \hat{X}} \phi_1 \left(\frac{\hat{Y}_J^I}{h_2^n} \right) \phi_1 \left(\frac{\hat{Z}_J^I}{h_3^n} \right) + n_{yi} \phi_1 \left(\frac{\hat{X}_J^I}{h_1^n} \right) \frac{\partial \phi_1 \left(\frac{\hat{Y}_J^I}{h_2^n} \right)}{\partial \hat{Y}} \phi_1 \left(\frac{\hat{Z}_J^I}{h_3^n} \right) \\ &\quad + n_{zi} \phi_1 \left(\frac{\hat{X}_J^I}{h_1^n} \right) \phi_1 \left(\frac{\hat{Y}_J^I}{h_2^n} \right) \frac{\partial \phi_1 \left(\frac{\hat{Z}_J^I}{h_3^n} \right)}{\partial \hat{Z}} \quad i = 1, 2, 3 \end{aligned} \quad (39)$$

The computation of system of equations in Eq. (16) involves two coinciding stress points at each meshfree node, one for standard nodal stress $\boldsymbol{\sigma}$ and the other for the stabilization nodal stress $\tilde{\boldsymbol{\sigma}}$. This dual stress point integration scheme is illustrated in Fig. 2. Note the present study utilizes the convex approximation to approximate the solution in Eq. (5). Different from other coupling approaches in meshfree methods [47, 48], the convex approximation imposes weak Kronecker-delta property [39] on the boundary of problem domain as well as the coupling interfaces between FEM and SPG domains. Our previous dispersion error analysis analyses [43] indicate that the convex approximation minimizes the sampling aliasing and produces a better solution than standard non-convex approximation (such as approximations in EFG and RKPM methods) in Fourier transform domain. Our analysis [43] of full-discretization in the wave equations also indicates that convex approximation produce less amplitude error and phase error than standard meshfree approximation. Our other study [49] also suggests that convex approximation is able to generate a more stable solution, improve solution errors and reduce the wave reflections in a coupling method.

Finally, the critical time step for the central difference time integration in the explicit

dynamics analysis is governed by the Courant-Friedrichs-Lewy (CFL) condition and is determined following the development in [34, 36, 43] for our numerical study. With the additional stabilization term, the critical time step Δt_c is modified according to the eigenvalue inequality theorem [50] to become

$$\Delta t_c = \frac{2}{\sqrt{\max_{l=1, NP}(\lambda_{\max}^l)}} \quad (40)$$

$$\lambda_{\max}^l \leq c_d^2 \max \left(\sum_{J=1}^{NP} \frac{\phi_{J,x}^2(\hat{\mathbf{X}}_l) + A_J(\hat{\mathbf{X}}_l)}{\phi_J(\hat{\mathbf{X}}_l)}, \sum_{J=1}^{NP} \frac{\phi_{J,y}^2(\hat{\mathbf{X}}_l) + A_J(\hat{\mathbf{X}}_l)}{\phi_J(\hat{\mathbf{X}}_l)}, \sum_{J=1}^{NP} \frac{\phi_{J,z}^2(\hat{\mathbf{X}}_l) + A_J(\hat{\mathbf{X}}_l)}{\phi_J(\hat{\mathbf{X}}_l)} \right) \quad (41)$$

$$A_J(\hat{\mathbf{X}}_l) = \tilde{b}_{J1}^2(\hat{\mathbf{X}}_l) + \tilde{b}_{J2}^2(\hat{\mathbf{X}}_l) + \tilde{b}_{J3}^2(\hat{\mathbf{X}}_l) \quad (42)$$

where $c_d = \sqrt{\frac{E(1-d)(1-\nu)}{(1+\nu)(1-2\nu)\rho}}$ is the material sound speed for damage model. E and ν denote the Young's modulus and Poisson's ratio respectively. The spatial derivatives of the Lagrangian shape function in inequality (41) are computed using the chain rule given by

$$\phi_{J,i}(\mathbf{X}) = \phi_{J,i}^0 = \frac{\partial \phi_J^0}{\partial x_i} = \frac{\partial \phi_J^0}{\partial X_j} \frac{\partial X_j}{\partial x_i}, i = 1, 2, 3 \quad (43)$$

The explicit dynamic analysis using Equation (40) gives a conservative estimation of critical time step but very stable results in the nodal integration method. It is worthwhile to note that the meshfree time steps in the explicit dynamics analysis are controlled implicitly [34, 36, 43] by the radius size a of $\phi_l^a(\mathbf{x})$ from the adaptive anisotropic Lagrangian kernel instead of the closet nodal distance or element size in finite element method; therefore they will not be cut down abruptly due to severe material deformation.

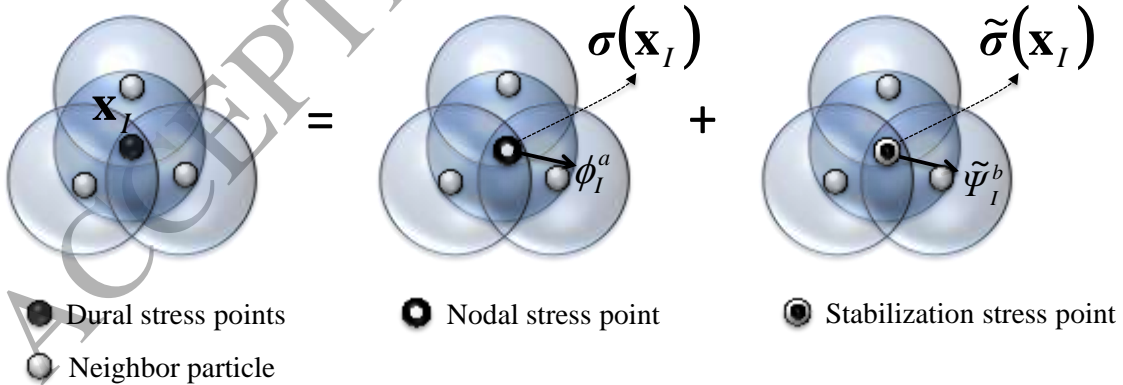


Fig. 2. Illustration of dual stress points in the present method.

4. Concrete Model and Failure Analysis

This section describes a regularized constitutive model for the failure analysis of concrete material under the dynamic loading conditions. The material modeling of concrete behavior is critical to the success of numerical prediction of the impact characteristics of a projectile on a concrete target. The most frequently used phenomenological concrete model accounts for elastic-plastic deformation, damage, hydrostatic stress and strain-rate effects, as an extension of the metal plasticity model [51, 52].

The phenomenological model developed by Malvar et al [51], named as the Karagozian & Case concrete (KCC) model, has been evaluated and validated by many users for both pretest predictions and posttest validations [53 – 60]. Through these studies, the KCC model has been proven to be able to physically capture the concrete responses under quasi-static, high frequency blast, impact, and ballistic loadings. Therefore, it is employed in this study to describe the concrete behaviors.

4.1. Concrete strength surfaces

The KCC model employs three independent, pressure sensitive strength surfaces to establish the strength, $\Gamma(p, J_3, \lambda)$, of the concrete, which is defined as:

$$\Gamma(p, J_3, \lambda) = \begin{cases} r_f \cdot \Theta(J_3) \cdot [\eta(\lambda) \cdot (\hat{\sigma}_m(p) - \hat{\sigma}_y(p)) + \hat{\sigma}_y(p)] & \lambda \leq \lambda_m \\ r_f \cdot \Theta(J_3) \cdot [\eta(\lambda) \cdot (\hat{\sigma}_m(p) - \hat{\sigma}_r(p)) + \hat{\sigma}_r(p)] & \lambda \geq \lambda_m \end{cases} \quad (44)$$

The strain rate enhancement is imposed through a user input dynamic increase factor r_f . The dependence on the third invariant (J_3) of the deviatoric stress is introduced to capture the difference between triaxial extension and compression behaviors and $\Theta(J_3)$ takes the form proposed by Willam and Warnke [61]. The three independent strength surfaces are defined as:

$$\hat{\sigma}_i(p) = a_{0i} + \frac{p}{a_{1i} + a_{2i}p} \quad i = m, y, r \quad (45)$$

The three strength surfaces in Eq. (44) and Eq. (45), namely, $\hat{\sigma}_m$, $\hat{\sigma}_y$, and $\hat{\sigma}_r$, are called the maximum, yield and residual strength surfaces respectively. The nine parameters to define these surfaces (i.e., a_{0i} , a_{1i} , and a_{2i} in Eq. (45) should be calibrated from experimental data.

Eq. (44) reveals that the concrete strength is interpolated between either $\hat{\sigma}_y$ and $\hat{\sigma}_m$ or $\hat{\sigma}_m$ and $\hat{\sigma}_r$ through the factor $\eta(\lambda)$. $\eta(\lambda)$ is a monotonic function of the modified plastic strain λ . The relationship between η and λ is calibrated through experimental data. A typical $\lambda - \eta$ relationship is shown in Fig. 3, which also discloses that $\eta(\lambda_m) = 1.0$. Fig. 3 also shows that η increases monotonically from 0.0 to 1.0 as λ increases from 0.0 to λ_m and decreases monotonically from 1.0 to 0.0 as λ increases from λ_m to λ_∞ . The former indicates the failure surface migrates from the yield strength surface to the maximum strength surface (strain

hardening process) and the latter implies the failure surface evolves from the maximum strength surface towards the residual strength surface (strain softening process).

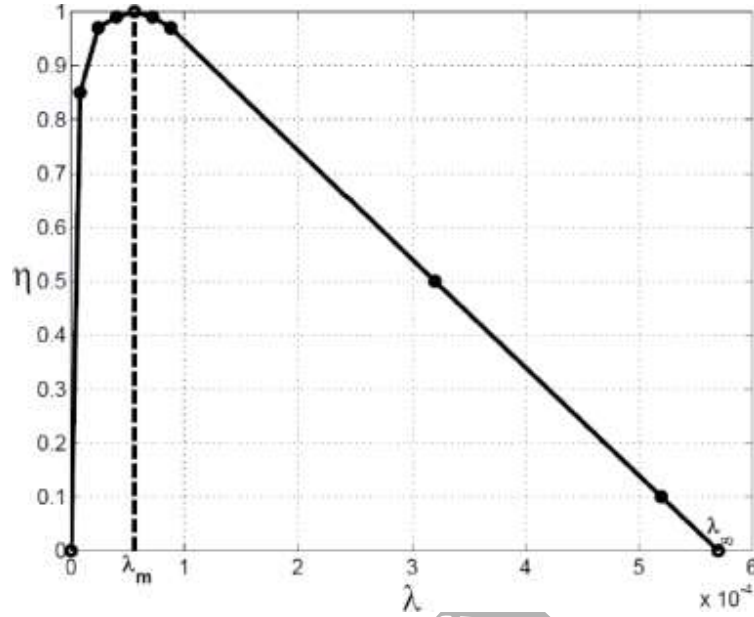


Fig. 3. Typical $\lambda - \eta$ relationship for the KCC model.

4.2. Plastic behavior

The plastic behavior in the KCC model is defined through the classical von-Mises plasticity theory. The yield function is formulated as:

$$\Upsilon(p, \boldsymbol{\sigma}, \lambda) = \sqrt{3J_2} - \Gamma(p, J_3, \lambda) \leq 0 \quad (46)$$

On the other hand, the KCC model introduces partial associativity to account for pressure induced by plastic flows at different levels, which leads the plastic potential to be written as:

$$\varphi(\boldsymbol{\sigma}, p, \lambda) = \sqrt{3J_2} - \varpi \Gamma(p, J_3, \lambda) \quad (47)$$

where ϖ is the associativity parameter.

The evolution of λ is defined as a function of the rate of plastic strain tensor:

$$\dot{\lambda} = h(p) \dot{\bar{\varepsilon}}^p \quad (48)$$

with $\dot{\bar{\varepsilon}}^p = \sqrt{\frac{2}{3} \dot{\boldsymbol{\varepsilon}}^p : \dot{\boldsymbol{\varepsilon}}^p}$, and the strain hardening factor $h(p)$ is defined as:

$$h(p) = \begin{cases} \left(1 + p / (r_f f_t)\right)^{-b_1} / r_f & p \geq 0 \text{ (compression)} \\ \left(1 + p / (r_f f_t)\right)^{-b_2} / r_f & p < 0 \text{ (tension)} \end{cases} \quad (49)$$

with b_1 and b_2 being the material parameters calibrated from test data for compression and tension respectively, and f_t is the tensile strength of the concrete. The b_1 and b_2 are also the regularization parameters used in the KCC model to alleviate discretization dependence, which will be demonstrated in a later example.

Following the standard return-mapping algorithm [62], the increment of the modified plastic strain ($\Delta\lambda$) can be obtained as:

$$\Delta\lambda = \frac{\Upsilon_{n+1}^{trial}}{(\Gamma_{,\lambda})_{n+1}^{trial} + h^{-1}(p_{n+1}^{trial}) \left[3G + \varpi K (\Gamma_{,p}^2)_{n+1}^{trial} \right] \left[1 + 2 \left(\frac{\varpi (\Gamma_{,p})_{n+1}^{trial}}{3} \right)^2 \right]^{-1/2}} \quad (50)$$

where G and K are shear and bulk modulus respectively.

As a result, the modified plastic strain can be accumulated as:

$$\lambda_{n+1} = \lambda_n + \Delta\lambda \quad (51)$$

Finally, the damage variable d introduced in Eq. (8) is defined as:

$$d = \left(1 + \frac{\lambda_m}{\lambda} \right)^{-1} \quad (52)$$

Since λ is a monotonic function of the effective plastic strain $\bar{\varepsilon}^p$, d is a monotonic function of the effective plastic strain $\bar{\varepsilon}^p$ as well. $d = 0.0$ when there is no plastic deformation, $d = 0.5$ when it hardens to the maximum strength surface ($\lambda = \lambda_m$), and $d \rightarrow 1.0$ when it softens to the residual strength surface ($\lambda \geq \lambda_\infty$).

4.3. Model Regularization

Concrete is a strain softening material, and therefore pathological discretization dependence will inevitably occur numerically. To alleviate this discretization dependence, the KCC model defines the discretization dependent damage evolution parameters b_1 and b_2 for compressive and tensile damage evolution respectively. With regularized b_1 and b_2 , relatively discretization independent results can be obtained.

Fig. 4 shows the stress – strain responses obtained with the proposed SPG formulation and the KCC model with b_1 regularization compared with the experimental data. The legend shows the shortest nodal distance of the SPG particles. The test performed is an unconfined uniaxial

compression (UUC) of a plain concrete cylinder. The concrete has an unconfined compressive strength of 45.4 MPa. The numerical results are close to the test data for different discretizations.

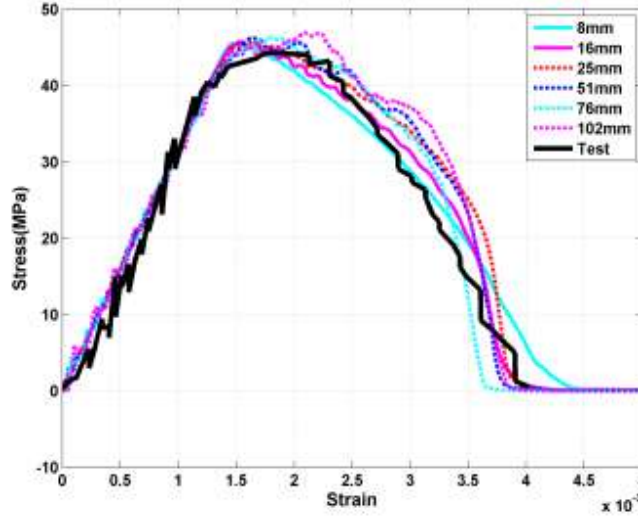


Fig. 4. Stress-strain responses for UUC tests by SPG.

Fig. 5 demonstrates the displacement – fracture energy and displacement – stress responses for an unconfined uniaxial tension (UUT) test of a plain concrete material. The concrete has an unconfined compressive strength of 45.4 MPa and a fracture energy of 80.2 N/m. The numerical results are obtained with the proposed SPG formulation and the KCC model with b_2 regularization, except the last one, which is obtained with the FE formulation. Once again, the legend shows the shortest nodal distance of the meshfree particles. The numerical results are obtained from single element simulations. The figure reveals that although the displacement – stress responses differ significantly, each element can dissipate about the same amount of fracture energy, which is the major interest for the analysis of this type of problem.

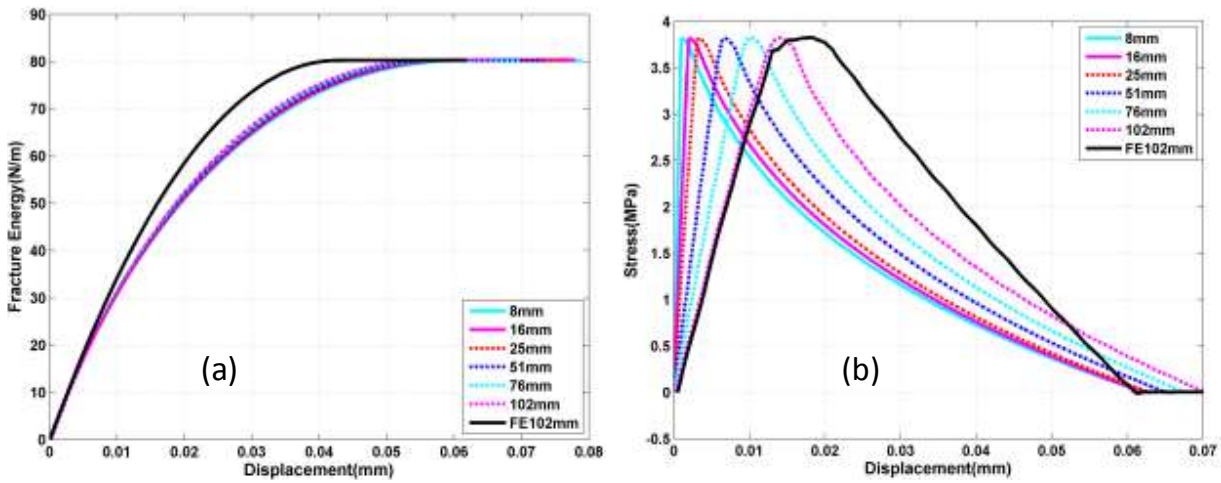


Fig. 5. Responses for UUT tests by SPG: (a) fracture energy, (b) stress.

4.4. Failure Analysis

It is worthwhile noting that we have to limit the damage variable to be bounded by $d < 1$ such that the fully damage ($d = 1$) does not occur. This is because the continuous problem is defined only when $0 \leq d < 1$. When $d = 1$ in Eq. (52) occurs, the modified plastic strain becomes infinite which is incomputable. In other words, if $d = 1$ is allowed in the damage model, the displacement discontinuities will be initiated. As a result, a crack will be formed and a strain singularity will thus be unavoidable at the crack tip. Numerically, this can be avoided by limiting the damage valuable d to a small value before fully damage. In this study a simple way to determine the value is to perform UUC and UUT tests. Fig. 6 shows the normalized material strength – damage responses. The material strength determined by Eq. (44) is normalized by its unconfined compressive and tensile strength respectively. The damage is calculated by Eq. (52). It can be observed that the material strength is about 40% of its original strength when the damage is up to 98.5%, and less than 5% when the damage is about 99%.

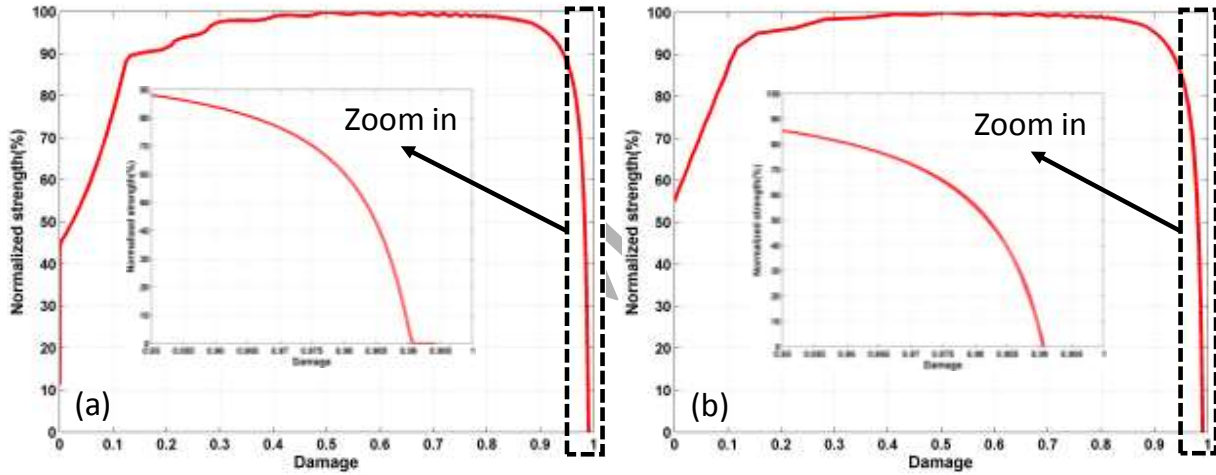


Fig. 6. Normalized strength vs damage: (a) UUC, (b) UUT.

On the other hand, excessive straining may arise under severe deformation since the material across the damage zone remains kinematically connected at almost zero stress levels [68]. As a result, the discontinuity is prohibited in the displacement field that leads to spurious damage growth in the severe deformation analysis. To prevent this non-physical behavior in the solution, two neighbor particles are considered disconnecting during the neighbor particle searching whenever their averaged damage value reaches a critical value. This numerical treatment is similar to the bond failure in peridynamics [46, 63, 64] method that avoids an explicit representation of the crack surface in 3D problem. In other words, we can redefine the three-dimensional ellipsoidal cubic spline kernel function in Eq. (36) for a pair of particles I and J to be

$$\phi(\hat{\mathbf{X}}_J - \hat{\mathbf{X}}_I) = \begin{cases} \phi_1\left(\frac{\hat{\mathbf{X}}_J^I}{h_1^n}\right)\phi_1\left(\frac{\hat{\mathbf{Y}}_J^I}{h_2^n}\right)\phi_1\left(\frac{\hat{\mathbf{Z}}_J^I}{h_3^n}\right) & \text{if } \hat{\mathbf{X}}_J \in \text{supp}(\phi_a^I) \text{ and } \frac{(d(\hat{\mathbf{X}}_I) + d(\hat{\mathbf{X}}_J))}{2} < d^{crit} \\ 0 & \text{if } \hat{\mathbf{X}}_J \notin \text{supp}(\phi_a^I) \text{ or } \frac{(d(\hat{\mathbf{X}}_I) + d(\hat{\mathbf{X}}_J))}{2} \geq d^{crit} \end{cases} \quad (53)$$

Because the damage variable d at each particle is monotonically increasing during the course of deformation, the disconnection between two particles in a pair is considered a permanent and irreversible process. This is an important characteristic of the present method in solid mechanics applications since the non-physical material self-healing issues can be completely exempted from the failure analysis.

Additionally, a frictionless self-contact algorithm is considered in this study to model the interaction between fully damaged concrete particles. Let \mathbf{x}_I and \mathbf{x}_J be the position vectors for particle I and particle J respectively. The normal gap in particle-to-particle contact algorithm is given by

$$\mathbf{g}_n^I = \mathbf{g}^I \cdot \mathbf{n}^I = (\mathbf{x}_J - \mathbf{x}_I) \cdot \frac{\mathbf{x}_{IJ}}{\|\mathbf{x}_{IJ}\|} = \|\mathbf{x}_{IJ}\| \quad \forall \mathbf{x}_J \in \text{supp}(\phi_a^I) \quad (54)$$

where $\mathbf{n}^I = \frac{\mathbf{x}_{IJ}}{\|\mathbf{x}_{IJ}\|}$ is the normal unit vector of the particle-to-particle contact pair, $\mathbf{g}^I \equiv \mathbf{x}_{IJ} = \mathbf{x}_J - \mathbf{x}_I$ defines corresponding gap function as shown in Fig. 7 and $\|\cdot\|$ is the associate norm representing the distance between two particles. For each penetrating slave particle J , the penalty force required to cancel the penetration to master particle I is evaluated by

$$\mathbf{f}_{IJ,n}^{scont} = p_n \mathbf{g}_n^I \mathbf{n}^I \quad \text{if } \mathbf{v}_{IJ} \cdot \frac{\mathbf{x}_{IJ}}{\|\mathbf{x}_{IJ}\|} > 0 \quad (55)$$

where p_n is the penalty number to enforce the normal contact and is taken as $p_n = 0.01 * E$ in this study. E is the Yong's modulus in concrete material. It is apparent that we have $\mathbf{f}_{IJ,n}^{scont} = -\mathbf{f}_{JI,n}^{scont}$ which satisfies the Newton's third law for particle interactions. Finally, the resultant frictionless contact force for particle I is calculated by

$$\mathbf{f}_{I,n}^{scont} = \sum_{J \neq I}^{NP} \mathbf{f}_{IJ,n}^{scont} = \sum_{J \neq I}^{NP} p_n \mathbf{g}_n^I \mathbf{n}^I \quad \forall \mathbf{x}_J \in \text{supp}(\phi_a^I) \text{ and } \mathbf{v}_{IJ} \cdot \frac{\mathbf{x}_{IJ}}{\|\mathbf{x}_{IJ}\|} > 0 \quad (56)$$

Eq. (56) is added into the right hand side of Eq. (16) to consider the self-contact effect for modeling the interaction between concrete debris in damage.

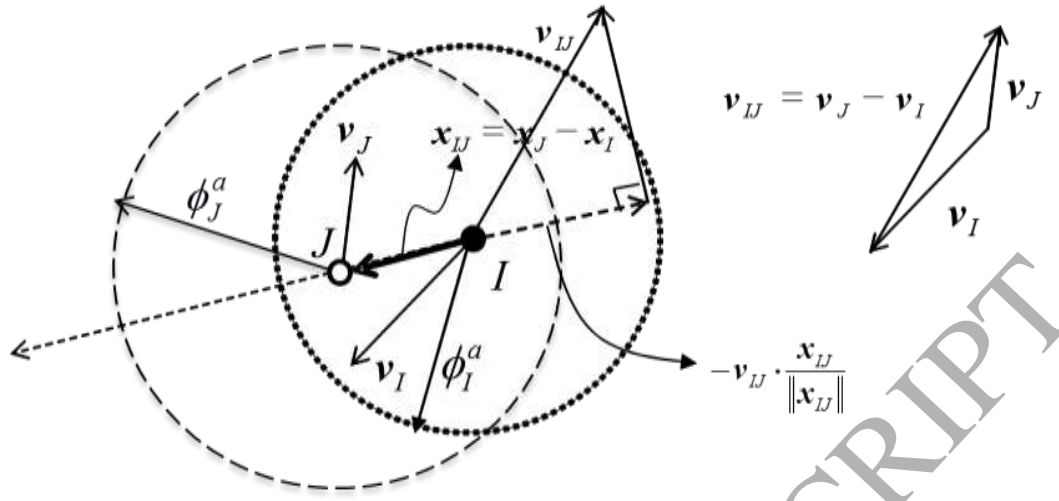


Fig. 7. Schematic sketch of two particles in contact.

5. Numerical Example

In this section, we evaluate the numerical performance of the proposed method for the simulation of three-dimensional concrete impact and penetration problems. One perforation test and one penetration test performed by Unosson and Nilsson [53] are analyzed herein. The projectile used in the tests is armor piercing steel projectile with a mass of 6.3 kg. The projectile, which has an ogival nose radius of 127 mm, a total length of 225 mm and a diameter of 75 mm, was fired perpendicularly to the center of the cylindrical specimen. The concrete specimen is made of high strength concrete with an unconfined compressive strength of 153 MPa and density of 2770 kg/m³.

5.1. Perforation Responses

In the perforation test, the concrete specimen has a diameter of 1400 mm and a length of 400 mm. The projectile was fired at a velocity of 621 m/sec towards the center of the specimen. The geometry and discretization of the model are shown in Fig. 8 where the black object is the projectile that is modeled by the finite element method with elastic material. Since the material failure in an impact penetration event is usually very localized, the immediate area under the projectile impact is modeled by the present method in this test while the rest of the concrete specimen can be modeled by finite element method to save computational cost. As such, a total number of 44649 SPG particles and 391040 elements (FE) are used to discretize the concrete specimen, which results in a total number of 447761 nodes for the discretization. The target is modeled by the KCC model with an associativity level of 0.5 and other material constants determined according to Ref. [60]. The perimeter of the specimen is set to be free. The penalty-based node-to-surface contact algorithm is employed to model the contact interaction between the projectile and the concrete specimen. The coefficient of friction between the projectile and the concrete is 0.10. A normalized nodal support size of 1.4 is utilized for the meshfree approximation and displacement smoothing. The adaptive anisotropic Lagrangian kernel is updated constantly every 30 explicit time steps.

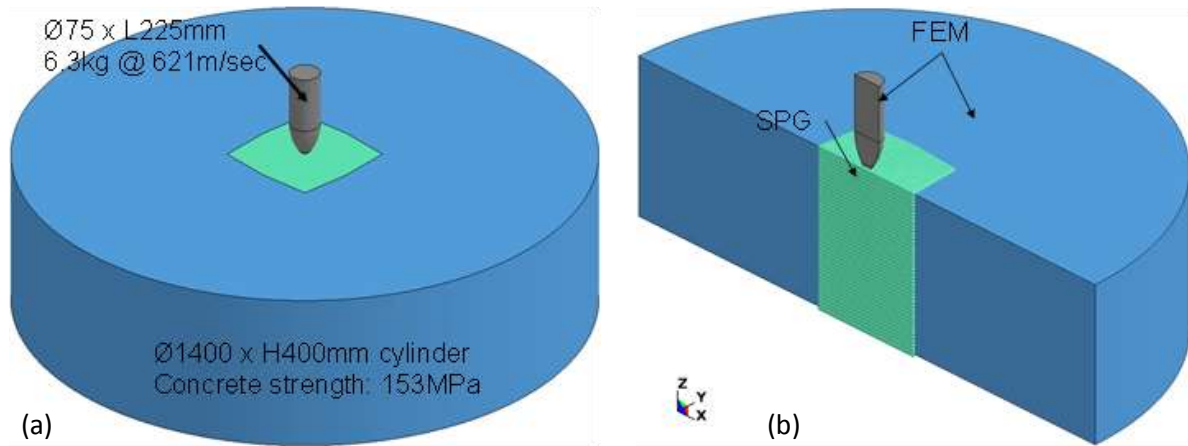


Fig. 8. Model for perforation response analysis: (a) dimension, (b) schematic discretization.

Fig. 9 compares the numerical and the experimental projectile velocity histories. Very nice agreement is observed between the two results. Fig. 9 also reveals that a relatively constant deceleration is obtained in both the numerical and the experimental results, which is a typical phenomenon in high velocity impact penetration / perforation tests. It is seen from the penetration depth – projectile velocity response in Fig. 9 (b) that the projectile moves at a relatively constant velocity after the penetration depth beyond 400 mm, which is the thickness of the target. This further verifies the perforation behavior of this test. Fig. 10 shows the energy profile obtained from the numerical analysis. The energy is normalized to the original total energy. The loss in the total energy is limited, therefore, the energy is preserved.

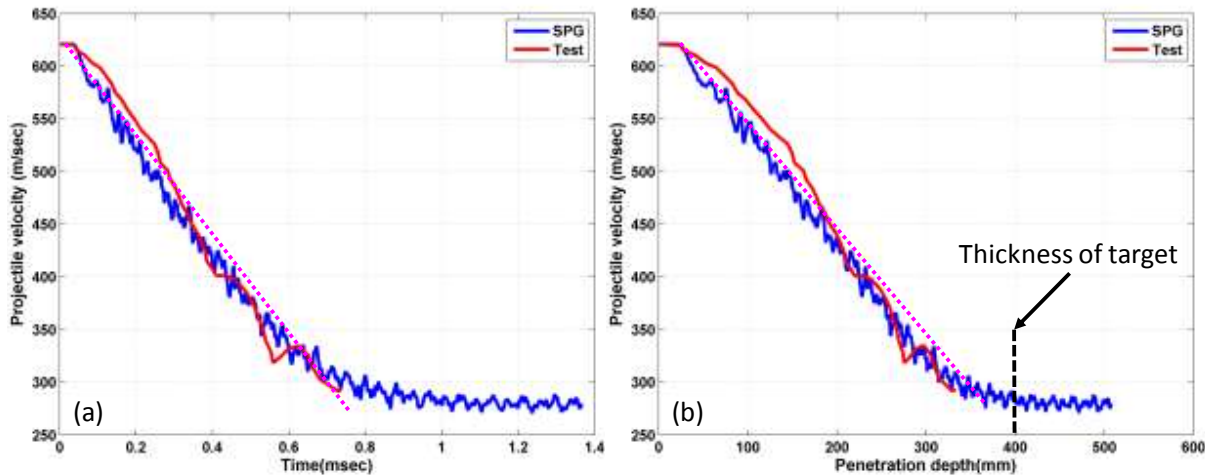


Fig. 9. Perforation responses: (a) projectile velocity time history, (b) history of projectile velocity vs penetration depth.

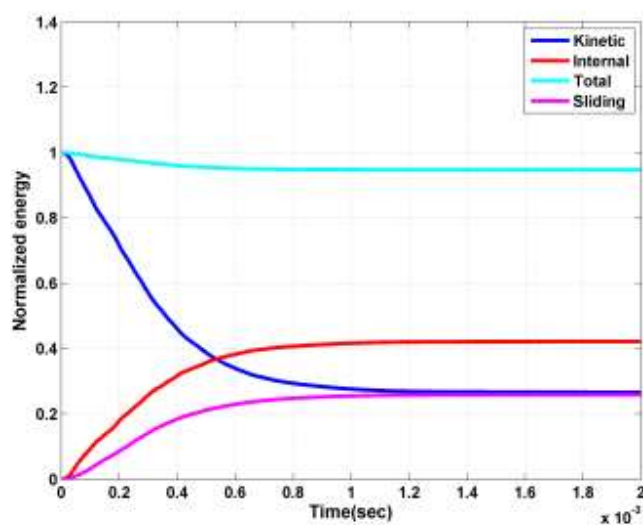


Fig. 10. Perforation responses: energy profile

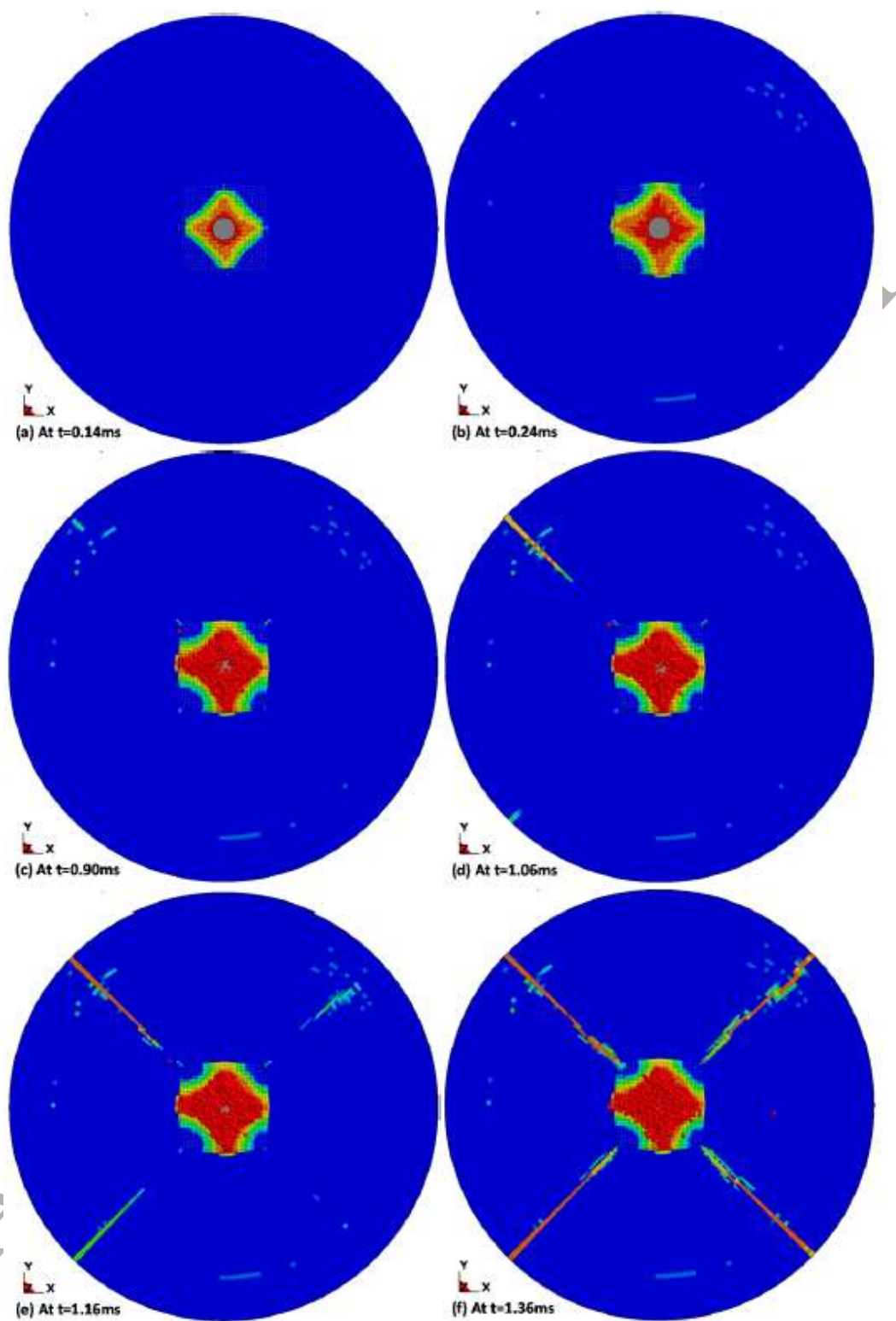




Fig. 11. Perforation responses: crack propagation.

Fig. 11 depicts the top view of radial crack initiation and propagation during the perforation process. The legend is the damage variable defined in Eq. (52) and this applies to all the other fringe plots in this paper. The fringe levels are defined in Fig. 11 (g) and this applies to all the other fringe plots in this paper as well. Fig. 11 shows that compressive damage reaches the edge of SPG zone at about 0.14 ms, and then circumferential damage bands far away from the impact zone were formed at about 0.24 ms due to reflected rarefaction tensile wave from the free outer surface. No significant evolution was found on the circumferential damage bands until termination of the analysis at 1.36 ms. The first micro radial crack was initiated at about 0.90 ms. A second micro radial crack was formed at about 1.06 ms, and the third and fourth micro radial cracks were initiated at about 1.16 ms. The micro radial cracks are finally developed into macro cracks at 1.36 ms, when the simulation was terminated while the projectile was observed to have perforated the target. The pattern of the radial crack propagation is consistent with many experimental observations [65].

Fig. 12 demonstrates the evolution of the plug cone where the section view at the central plane of the concrete specimen is plotted. The damage plug is another typical phenomenon observed in the perforation tests [66]. Fig. 12 shows that damage occurs immediately at 0.02 ms once the projectile – target contact is constructed, and then damage is initiated far away from the impact zone at 0.18 ms, which is due to the reflected rarefaction tensile wave while concrete has a very low tensile strength. The damage evolves from both sides (due to tension and compression respectively) and meets at 0.38 ms and forms the prototype of the plug cone. Meanwhile, ejecta and debris are first observed at this time, and they are observed more and more until termination of the analysis at 1.36 ms. As the projectile further penetrates through the specimen, the plug cone expands a little bit and reaches its final shape at about 0.88 ms. Meanwhile, the damage zone is expanded farther to the side of the projectile. The expanded damage zone further develops as the projectile tip penetrates through the concrete at 1.00 ms. The damage zone then further develops until termination at 1.36 ms while a stable residual velocity has reached. However, no other macro crack is formed. Fig. 12 also verifies that the damage in the high velocity impact penetration processes is very localized.

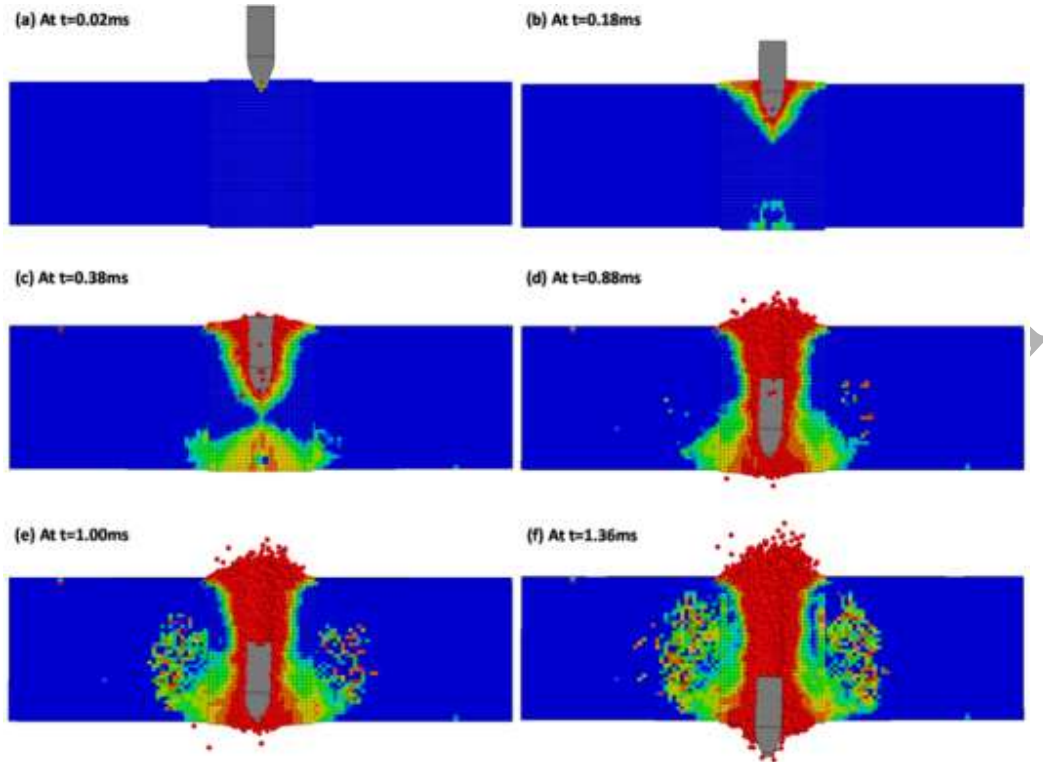


Fig. 12. Perforation responses: plug cone evolution.

To study the convergence performance of the proposed algorithm, a refined model is used for the simulation. In the refined model, transition elements (see Fig. 13(b)) are used to save computational cost. As a result, a total of 109181 SPG nodes and 62400 FE elements are used to discretize the target. Noticing the fact that damage and failure occurred very localized in this type of problem, the refinement is only applied to the region near the projectile tip, so that there are 17 nodes (see Fig. 13(d)) covered by the projectile, whereas in the coarse discretization, the number of covered nodes is 9 (see Fig. 13(c)). The discretization of the projectile is not changed. It should be pointed out that an even coarser discretization is not recommended since otherwise too few nodes will be covered by the projectile and thus the contact interaction will not be well captured. Fig. 14 shows the comparison of velocity histories obtained with coarse and fine discretizations and the experimental data. Very nice agreement is observed. The overall responses are also consistent with the results reported by Rabczuk and Belytschko [67] using an adaptive SPH scheme. Meanwhile, less oscillation is observed for the fine discretization, which seems to match even better with test data than the coarse discretization one. It should also be pointed out that in another study we found that bigger size of the meshfree zone does not significantly change the numerical responses, therefore, the results are not included in this paper.

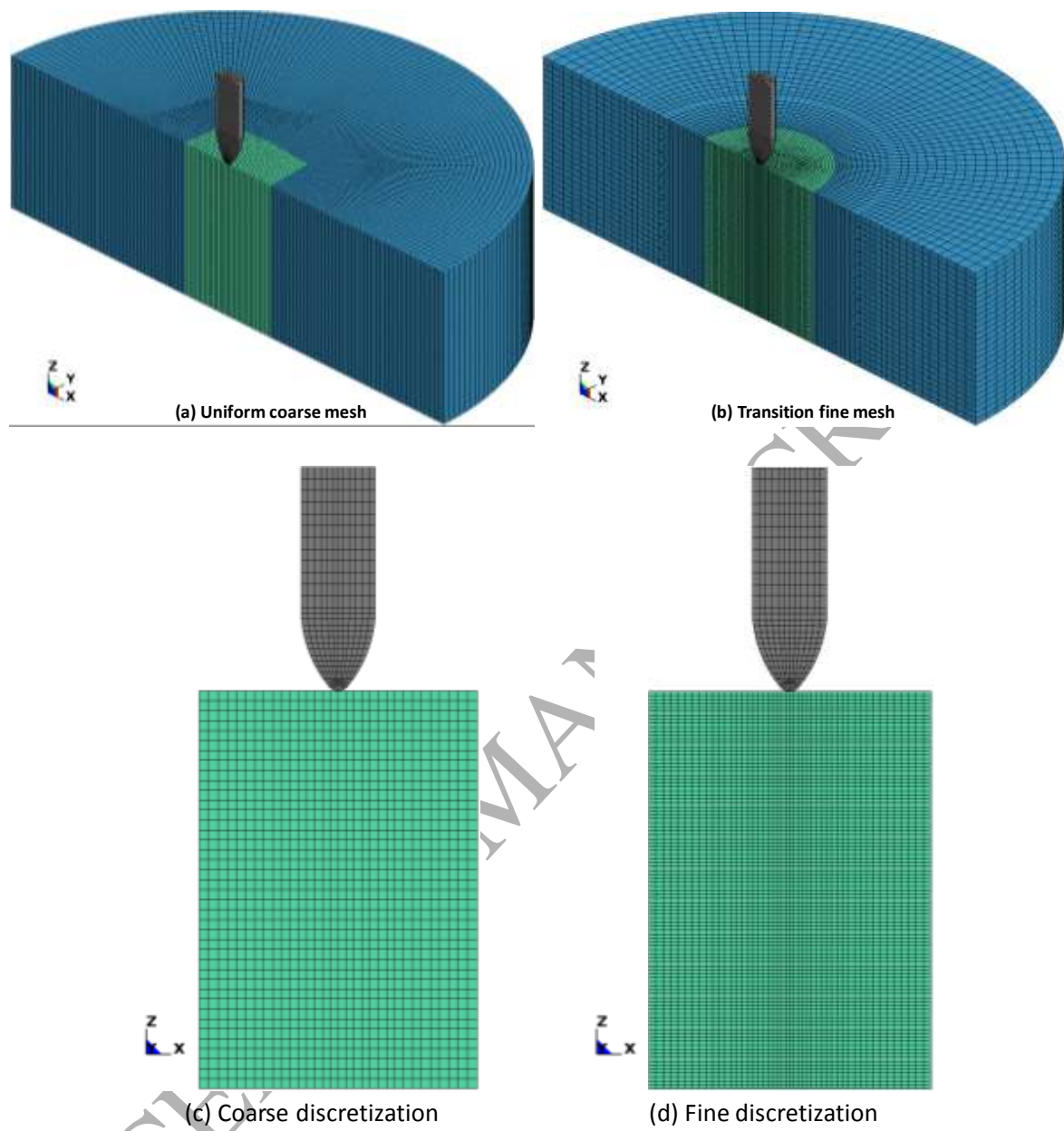


Fig. 13. Perforation responses: refined discretization

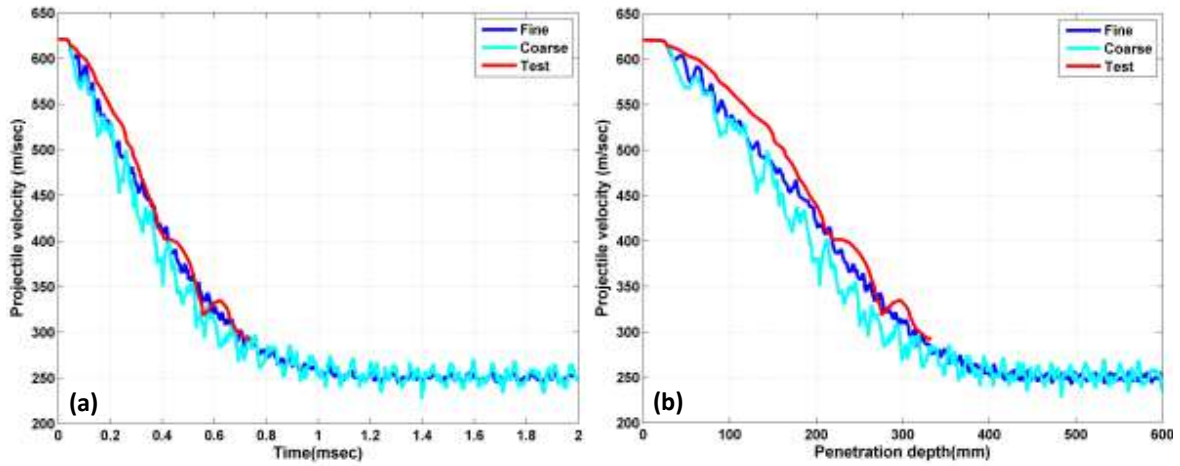


Fig. 14. Perforation responses with refined discretization: (a) projectile velocity time history, (b) history of projectile velocity vs penetration depth.

5.2. Penetration Analysis

In the penetration test, the specimen has a diameter of 1400 mm and length of 800 mm. The projectile was fired at a velocity of 623 m/sec towards the center of the specimen. The geometry and discretization of the model is shown in Fig. 15. Similar to the perforation test, only a small region of the concrete target right under the projectile is discretized by the present method and the rest of area is modeled by finite element method. In detail, 88209 SPG particles and 782080 elements (FE) are employed to discretize the target, which contains a total number of 884601 nodes. All the other numerical setups including material parameters in this test are the same as those for the perforation analysis.

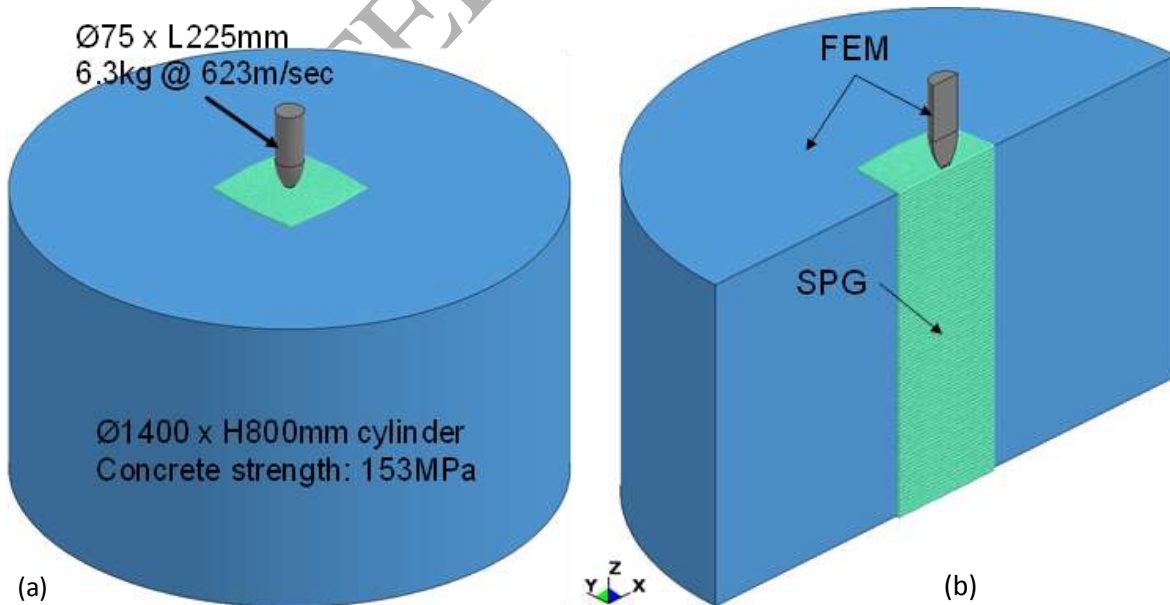


Fig. 15. Model for penetration analysis: (a) dimension, (b) schematic discretization.

Fig. 16 shows the projectile velocity and penetration depth histories in comparison with the experimental data. As shown in Fig. 16, the numerical results match the experimental results very nicely within the reliable region of test data. A relatively constant deceleration is obtained in both the numerical and the experimental results. The zero residual velocity in the numerical analysis indicates that the response is penetration, i.e., the projectile stops in the specimen. In fact, it penetrates into the target about 498 mm and then stopped. The normalized energy is shown Fig. 17. It is observed that the loss of total energy is very small and therefore, the energy conservation is satisfied.

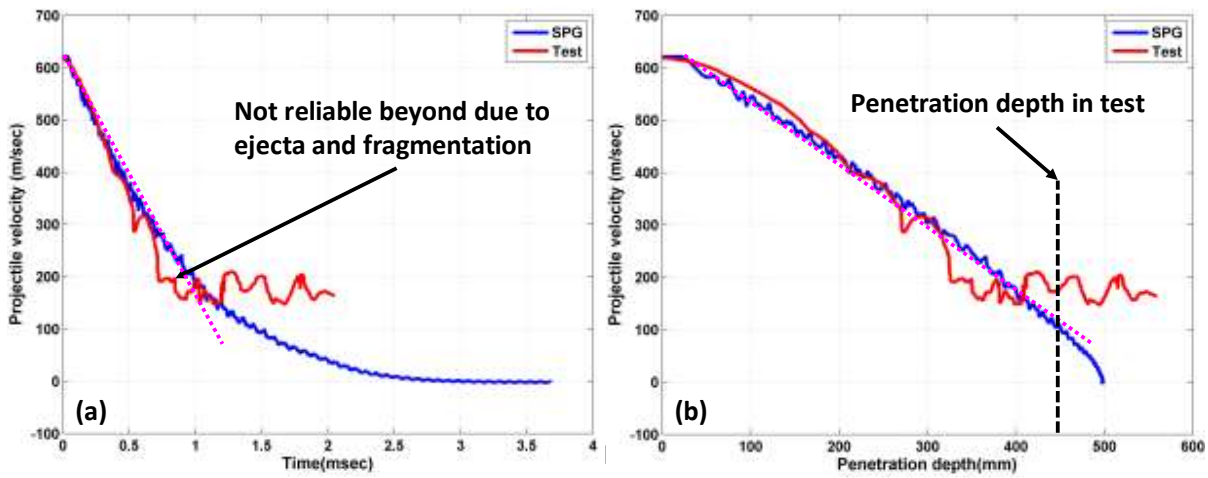


Fig. 16. Response of penetration: (a) projectile velocity time history, (b) history of projectile velocity vs penetration depth.

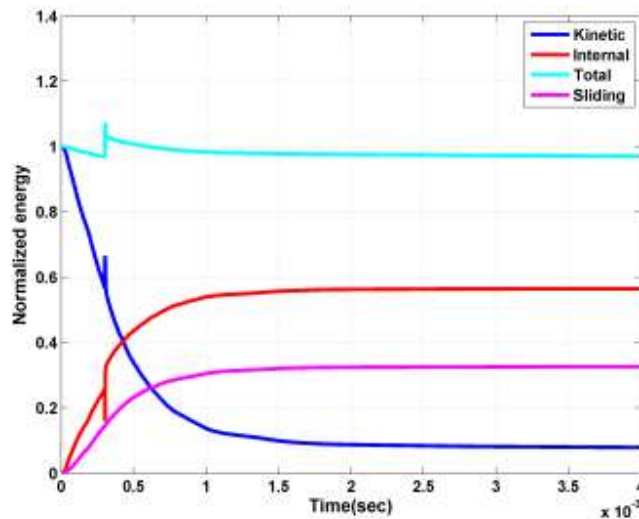


Fig. 17. Penetration responses: energy profile

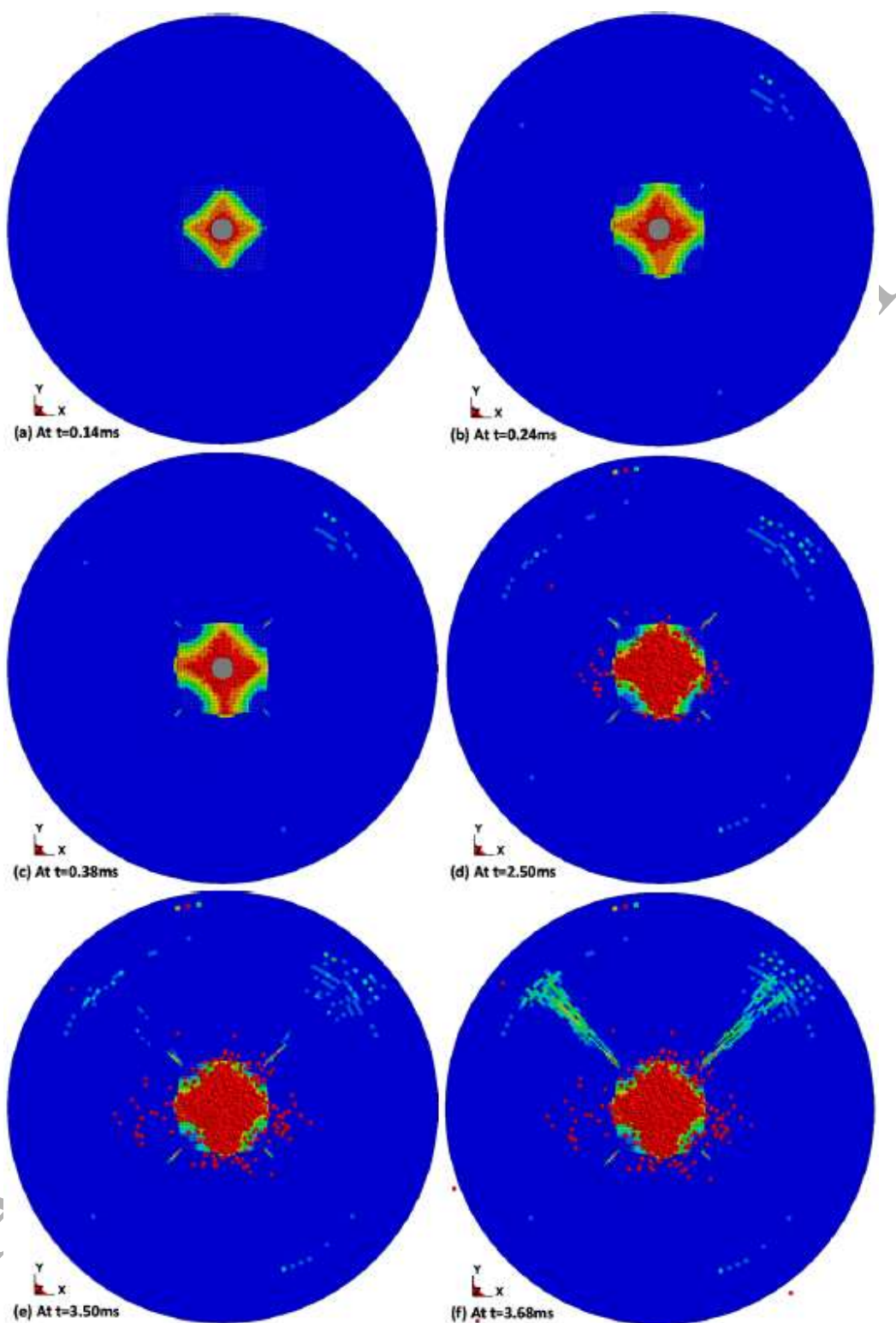


Fig. 18. Radial damage evolution in penetration response.

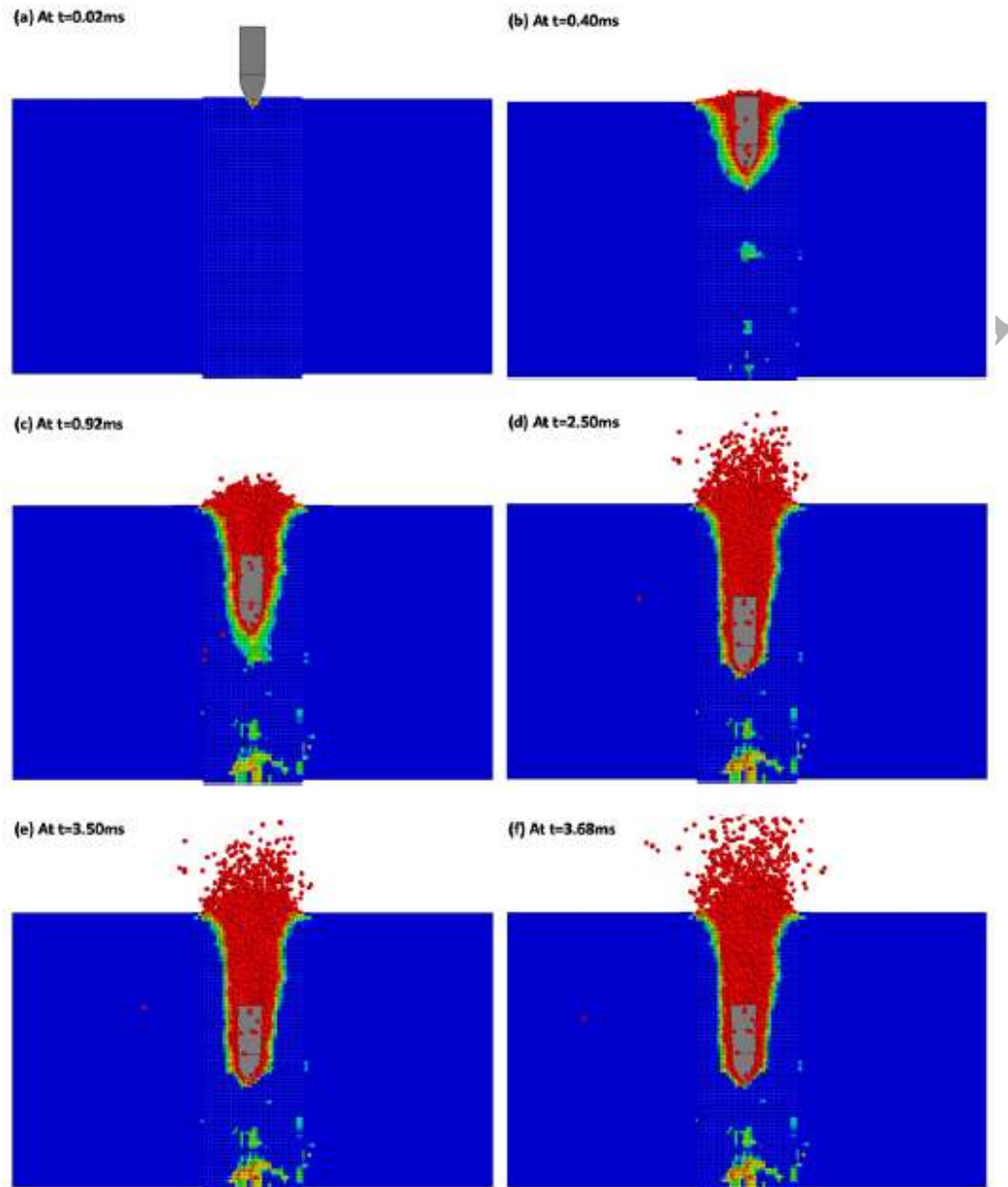


Fig. 19. Longitudinal damage evolution in penetration response.

Fig. 18 demonstrates the damage evolution in the cross – section view (on the impact face). It can be observed that damage spread out to the edge of meshfree zone at about 0.14 ms. Circumferential damage bands were noticed at around 0.24 ms, which is due to the reflected rarefaction tensile wave from the free outer surface. These damage bands were never developed enough to form macroscopic cracks until the end of simulation at 3.68 ms while the projectile has fully stopped. Radial damage bands were generated at about 0.38 ms. The radial damage bands seemed to have no significant development until 2.50 ms, and then a little evolution in the length at 3.50 ms. At the end of simulation at 3.68 ms, two long damage bands were observed. They are still called the damage bands because the damage level in these bands are not high

enough to form macroscopic cracks. This is due to the fact that the specimen is strong enough to absorb all the impact energy without macroscopic fracturing.

The longitudinal damage evolution is depicted in Fig. 19 for the penetration process on the section view through the central plane of the structure. Damage starts to accumulate right away when the projectile – target contact is initiated at 0.02 ms. Tensile damage is observed from the opposite face of the impact at around 0.40 ms. This is due to the reflection of the compressive impact wave from the free bottom surface, which forms a high pressure tensile wave. Meanwhile, ejecta and debris start to be observed at this time as well. More ejecta and debris are formed as the penetration process goes further until termination of the analysis at 3.68 ms when the projectile comes to a complete stop. It is also seen that the damage profile along the impact path away from the projectile tip (i.e., bottom portion of the target) is almost finalized at 0.92 ms since there is not much difference between solutions in this region for the rest of time until termination. This is because nearly 90% kinetic energy of the projectile has been absorbed by the concrete by 0.92 ms (c.f. Fig. 16). In comparison to the result in perforation test, there is no clear plug cone in this penetration response.

6. Conclusions

The numerical challenges in modeling the penetration and fragmentation of concretes consist in dealing with high levels of deformation and material failure involving in the complex material flow due to severe shock and impact loads. In this study, we have proposed an improved meshfree methodology for the prediction of fundamental structure response and projectile characteristics in the three-dimensional concrete impact and penetration problems. The present method focuses on the generalization of our previous development in two-dimensional large deformation analysis [34] to three-dimensional formulation. Additionally, in order to extend the three-dimensional large deformation formulation to the model of the material failure in concrete impact and penetration problems, a regularized concrete damage model is implemented together with an introduction of bond-based failure criterion and self-contact algorithm in the formulation.

The computational advantages offered by the present stabilized meshfree Galerkin method are very appealing. The numerical results in this study suggest that the present method is capable of delivering a stable solution that emulates the essential concrete response and projectile characteristics. In particular, the scabbing and perforation of concrete under high velocity impact are captured in the simulation. The present method also offers a great potential for solving modern impact and penetration problems when an immersed technique [68] are built-in for the formulation and the reinforced concretes are considered in the simulation. Further developments regarding such simulation will be discussed and presented in the near future.

Acknowledgements

The authors would like to thank Dr. John O. Hallquist of LSTC for his support to this research. Authors also wish to express their gratitude to researchers in Karagozian & Case Inc. for the helpful discussion.

References

- [1] Huerta A, Liu WK. Viscous flow with large free surface motion. *Computer Methods in Applied Mechanics and Engineering* 1998;69:277-324.
- [2] Chen JS, Pan C, Wu CT, Liu WK. Reproducing kernel particle methods for large deformation analysis of non-linear structures. *Computer Methods in Applied Mechanics and Engineering* 1996;139:195-227.
- [3] Li S, Liu WK. *Meshfree Particle Method*. Berlin: Springer Verlag; 2004.
- [4] Simkins DC, Li S. Meshfree simulation of thermo-mechanical ductile fracture. *Computational Mechanics* 2006;38:235-249.
- [5] Wu CT, Guo Y, Askari E. Numerical modeling of composite solids using an immersed meshfree Galerkin method. *Composites B* 2013;45:1397-1413.
- [6] Hentz S, Donze FV, Daudeville L. Discrete element modelling of concrete submitted to dynamic loading at high strain rates. *Computers and Structures* 2004;82:2509-2524.
- [7] Nguyen CT, Nguyen Chi T, Bui HH, Nguyen GD, Fukagawa R. A new SPH-based approach to simulation of granular flows using viscous damping and stress regularization. *Landslides* (2016). DOI: 10.1007/s10346-016-0681-y.
- [8] Monaghan JJ. Smoothed particle hydrodynamics. *Annual Review of Astronomy and Astrophysics* 1992;30:543-574.
- [9] Violeau D. *Fluid Mechanics and the SPH Method: Theory and Applications*. Oxford: Oxford University Press; 2012.
- [10] Belytschko T, Guo Y, Liu WK, Xiao SP. A unified stability analysis of meshless particle methods. *International Journal for Numerical Methods in Engineering* 2000;48:1359-1400.
- [11] Rabczuk T, Belytschko T, Xiao SP. Stable particle methods based on Lagrangian kernels. *Computer Methods in Applied Mechanics and Engineering* 2004;193:1035-1063.
- [12] Tham CY. Numerical and empirical approach in predicting the penetration of a concrete target by an ogive-nosed projectile. *Finite Elements in Analysis and Design* 2006;42:1258-1268.
- [13] Chizel-Marmot Y, Ortiz R, Combescure A. Three dimensional SPH-FEM gluing for simulation of fast impacts on concrete slabs. *Computers & Structures* 2011;89:2484-2494.
- [14] Huang XC, Yan YX, Zhong WZ, Chen YZ, Zhu JS. A numerical method for penetration into concrete target using SPH-Lagrangian coupling method. *Advanced materials Research* 2011;163-167:1217-1221.
- [15] Rabczuk T, Eibl J. Simulation of high velocity concrete fragmentation using SPH/MLSPH. *International Journal for Numerical Methods in Engineering* 2003;56:1421-1444.
- [16] Liu MB, Liu GR. Smoothed particle hydrodynamics (SPH): an overview and recent developments. *Archives of Computational Methods in Engineering* 2010;17:25-76.
- [17] Belytschko T, Lu YY, Gu L. Element-free Galerkin methods. *International Journal for Numerical Methods in Engineering* 1994;37:229-256.
- [18] Liu WK, Jun S, Zhang YF. Reproducing kernel particle methods. *International Journal for Numerical Methods in Fluids* 1995;20:1081-1106.
- [19] Cueto-Felgueroso L, Colominas I, Mosqueria G, Navarrina F, Casteleiro M. On the Galerkin formulation of the smoothed particle hydrodynamics method. *International Journal for Numerical Methods in Engineering* 2004;60:1475-1512.
- [20] Rabczuk T, Belytschko T. Cracking particles: a simplified meshfree method for arbitrary evolving cracks. *International Journal of Impact Engineering* 2004;61:2316-2343.
- [21] Belytschko T, Krongauz Y, Fleming M, Organ D, Liu WK. Smoothing and accelerated

- computations in the element free Galerkin method. *Journal of Computational and Applied Mathematics* 1996;74:111-126.
- [22] Barbiere E, Petrinic N. Three-dimensional crack propagation with distance-based discontinuous kernels in meshfree method. *Computational Mechanics* 2014;53:325-342.
- [23] Chen JS, Wu CT, Yoon S, You Y. A stabilized conforming nodal integration for Galerkin Meshfree methods. *International Journal for Numerical Methods in Engineering* 2001;50:435-466.
- [24] Duan Q, Li X, Zhang H, Belytschko T. Second-order accurate derivatives and integration schemes for meshfree methods. *International Journal for Numerical Methods in Engineering* 2012;92:399-424.
- [25] Chen JS, Hillman M, Ruter M. An arbitrary order variationally consistent integration for Galerkin meshfree methods. *International Journal for Numerical Methods in Engineering* 2013;95:387-418.
- [26] Wang D, Peng H. A Hermite reproducing kernel Galerkin meshfree for buckling analysis of thin plates. *Computational Mechanics* 2013;51:1013-1029.
- [27] Wang D, Wu J. An efficient nesting sub-domain gradient smoothing integration algorithm with quadratic exactness for Galerkin meshfree methods. *Computer Methods in Applied Mechanics and Engineering* 2016;298:485-519.
- [28] Puso MA, Chen JS, Zywicz E, Elmer W. Meshfree and finite element nodal integration methods. *International Journal for Numerical Methods in Engineering* 2008;74:416-446.
- [29] Sherburn JA, Roth MJ, Chen JS, Hillman M. Meshfree modeling of concrete slab perforation using a reproducing kernel particle impact and penetration formulation. *International Journal of Impact Engineering* 2015;86:96-110.
- [30] Wang D, Li Z. A two-level strain smoothing regularized meshfree approach with stabilized conforming nodal integration for elastic damage analysis. *International Journal of Damage Mechanics* 2013;22:440-459.
- [31] Wu Y, Wang D, Wu CT. Three dimensional fragment simulation of concrete structures with a nodally regularized meshfree method. *Theoretical and Applied Fracture Mechanics* 2014;72:89-99.
- [32] Wu Y, Wang D, Wu CT, Zhang H. A direct displacement smoothing meshfree particle formulation for impact failure modeling. *International Journal of Impact Engineering* 2016;87:169-185.
- [33] Wu CT, Koishi M, Hu W. A displacement smoothing induced strain gradient stabilization for the meshfree Galerkin nodal integration method. *Computational Mechanics* 2015;56:19-37.
- [34] Wu CT, Chi SW, Koishi M, Wu Y. Strain gradient stabilization with dual stress points for the meshfree nodal integration method in inelastic analysis. *International Journal for Numerical Methods in Engineering* 2016;107:3-30.
- [35] Wu CT, Wu Y, Koishi M. A strain-morphed nonlocal meshfree method for the regularized particle simulation of elastic-damage induced strain localization problems. *Computational Mechanics* 2015;56:1039-1054.
- [36] Wu CT, Ma N, Takada K, Okada H. A meshfree continuous-discontinuous approach for the ductile fracture modeling in explicit dynamics analysis. *Computational Mechanics* 2016;58:391-409.
- [37] Beissel S, Belytschko T. Nodal integration of the element-free Galerkin method. *Computer Methods in Applied Mechanics and Engineering* 1996;139:49-74.
- [38] Hughes TJR. *The Finite Element Method*. Englewood Cliffs, NJ: Prentice-hall, 2000.

- [39] Wu CT, Park CK, Chen JS. A generalized approximation for the meshfree analysis of solids. *International Journal for Numerical Methods in Engineering* 2011;85:693-722.
- [40] Wu CT, Koishi M. Three-dimensional meshfree-enriched finite element formulation for micromechanical hyperelastic modeling of particulate rubber composites. *International Journal for Numerical Methods in Engineering* 2012;91:1137-1157.
- [41] Wang D, Chen P. Quasi-convex reproducing kernel meshfree method. *Computational Mechanics* 2014;55:689-709.
- [42] Zhang H, Wang D. An isogeometric enriched quasi-convex meshfree formulation with application to material interface modeling. *Engineering Analysis with Boundary Elements* 2015;60:37-50.
- [43] Park CK, Wu CT, Kan CD. On the analysis of dispersion property and stable time step in meshfree method using the generalized meshfree approximation. *Finite Elements in Analysis and Design* 2011;47:683-697.
- [44] Belytschko T, Bindeman LP. Assumed strain stabilization of the eight node hexahedral element. *Computer Methods in Applied Mechanics and Engineering* 1993;105:225-260.
- [45] Hughes TJR, Winget J. Finite rotation effects in numerical integration of rate constitutive equations arising on large deformation analysis. *International Journal for Numerical Methods in Engineering* 1980;15:1862-1867.
- [46] Wu CT, Ren B. A stabilized non-ordinary state-based peridynamics for the nonlocal ductile material failure analysis in metal machining process. *Computer Methods in Applied Mechanics and Engineering* 2015;291:197-215.
- [47] Rabczuk T, Xiao SP, Sauer M. Coupling of meshfree methods with finite elements: Basic concepts and test results. *Numerical Methods in Biomedical Engineering* 2006;22:1031-1065.
- [48] Talebi H, Silani M, Bordas SPA, Kerfriden P, Rabczuk T. A computational library for multiscale modelling of material failure. *Computational Mechanics* 2014;53:1047-1071.
- [49] Wu CT. Kinematic constraints in the state-based peridynamics with mixed local/nonlocal gradient approximations. *Computational Mechanics* 2014;54:1255-1267.
- [50] Belytschko T, Liu WK, Moran B. *Nonlinear Finite Elements for Continua and Structures*. Chichester: Wiley; 2000.
- [51] Malvar LJ, Crawford JE, Wesevich JW, Simons D. A plasticity concrete material model for DYNA3D. *International Journal of Impact Engineering* 1997;19:847-873.
- [52] Meyers MA. *Dynamic behavior of materials*. New York: Wiley, 1994.
- [53] Unosson M, Nilsson L. Projectile penetration and perforation of high performance concrete: experimental results and macroscopic modeling. *International Journal of Impact Engineering* 2006;32:1068-1085.
- [54] ARUP, Verification of the Karagozian and Case material model for LS-DYNA 971 R3. London: 124857-07, Ove Arup & Partners Ltd; 2009.
- [55] Elsanadedy HM, Almusallam TH, Abbas H, Al-Salloum YA, Alsayed SH. Effect of blast loading on CFRP-Retrofitted RC columns – a numerical study. *Latin American Journal of Solids and Structures* 2011;8:55 – 81.
- [56] Hansra HS. 3-D finite element modeling of reinforced concrete beam-column connections – development and comparison to NCHRP project 12-74. Sacramento: thesis for master of science, California State University, Sacramento; 2012.
- [57] Li XQ, Chen JF, Lu Y. Meso-scale modeling of FRP-to-concrete bond behavior using LS-DYNA. In: Ye L, Feng P, Yue Q. *Advances in FRP Composites in Civil Engineering*, Beijing:

- Tsinghua University Press, and Berlin Heidelberg: Springer-Verlag; 2011, p 494-498.
- [58] Lin X, Zhang YX, Hazell PJ. Modelling the response of reinforced concrete panels under blast loading. *Materials and Design* 2013;56:620-628.
 - [59] Crawford JE. State of the art for enhancing the blast resistance of reinforced concrete columns with fiber-reinforced plastic. *Canadian Journal of Civil Engineering* 2013;40:1023-1033.
 - [60] Wu Y, Crawford JE. Numerical modeling of concrete using a partially associative plasticity model. *ASCE Journal of Engineering Mechanics*, 2015. [http://dx.doi.org/10.1061/\(ASCE\)EM.1943-7889.0000952](http://dx.doi.org/10.1061/(ASCE)EM.1943-7889.0000952).
 - [61] Willam KJ, Warnke EP. Constitutive model for the triaxial behavior of concrete. *Proceedings of International Association for Bridge and Structural Engineering (ISMES, Bergamo, Italy)* 1975;19:174-186.
 - [62] Simo JC, Hughes TJR. *Computational Inelasticity*. New York: Springer; 1998.
 - [63] Silling SA, Askari E. A meshfree method based on the peridynamic model of solid mechanics. *Computers and Structures* 2005;83:1526-1535.
 - [64] Ren B, Wu CT, Askari E. A 3D discontinuous Galerkin finite element method with the bond-based peridynamics model for dynamic brittle failure analysis. *International Journal of Impact Engineering* 2017;99:14-25.
 - [65] Hansson H. Warhead penetration in concrete protective structures. Stockholm, Sweden: Licentiate Thesis, Royal Institute of Technology; 2011.
 - [66] Bruhl JC, Varma AH, Johnson WH. Design of SC composite walls for projectile impact: local failure. San Francisco, CA: Transactions, SMiRT-22; 2013.
 - [67] Rabczuk T, Belytschko T. A three-dimensional large deformation meshfree method for arbitrary evolving cracks. *Computer Methods in Applied Mechanics and Engineering* 2007;196:2777-2799.
 - [68] Wu CT, Wang D, Guo Y. An immersed particle modeling technique for the three-dimensional large strain simulation of particulate-reinforced metal-matrix composites. *Applied Mathematical Modeling* 2016;40:2500-2513.